



# Evaluating the performances of cloud microphysical parameterizations in WRF for the heavy rainfall event of Kerala (2018)

Tapajyoti Chakraborty<sup>1</sup> · Sandeep Pattnaik<sup>1</sup> · R. K. Jenamani<sup>2</sup> · H. Baisya<sup>1</sup>

Received: 26 May 2020 / Accepted: 6 January 2021 / Published online: 22 January 2021  
© The Author(s), under exclusive licence to Springer-Verlag GmbH, AT part of Springer Nature 2021

## Abstract

This study evaluates the performances of four different cloud microphysical parameterization (CMP) schemes of the Weather Research and Forecasting (WRF) model at 3 km horizontal resolution (lead time up to 96 h) for the Heavy Rainfall Event (HRE) over Kerala in August 2018. The goal is to identify the major drivers for rain making mechanism and evaluate the ability of CMPs to accurately simulate the event with special emphasis on rainfall. It is found that the choice of CMP has a considerable impact on the rainfall forecast characteristics and associated convection. Results are validated against the India Meteorological Department (IMD) station data and Global Precipitation Measurement (GPM) observations and found that, among the four CMP schemes, viz., Milbrandt (MIL), Thompson Aerosol Aware (TAA), WRF double-moment 6-class scheme (WDM6) and WRF single-moment 6-class scheme (WSM6); WDM6 is the best performing scheme in terms of rainfall. It is noted that mixed phase processes are dominant in this scenario and the inability (ability) of MIL and TAA (WDM6 and WSM6) to predict the frozen hydrometeors, and thus simulating the cold rain processes realistically led to large (small) errors in the rainfall forecast. The moisture convergence was prominent in the foothills of the Western Ghats and highly influential in facilitating orography driven lifting of moisture. The moisture budget results suggest that horizontal moisture flux convergence (MFC) was the major driver of convection with WDM6 predicting the peaks of MFC most consistently with the observed Tropical Rainfall Measuring Mission (TRMM) rainfall product. Additionally, from Contiguous Rain Area analysis it is also found that the WDM6 has the least volumetric error. This is to highlight that hydrometeor distributions are strongly modulated by MFC, which further impacts the latent heat generation and rainfall over the region. Overall results infer the substantial influence of CMPs on the forecast of the Heavy Rainfall Event. The findings of this study will be highly useful for operational forecasting agencies and disaster management authorities for mitigation of damages caused by this kind of severe HREs in the future.

## Abbreviations

WRF	Weather research and forecasting	WDM6	WRF Double Moment 6-class Scheme
HRE	Heavy rainfall event	WSM6	WRF Single Moment 6-class Scheme
CMP	Cloud microphysical parameterization	MFC	Moisture flux convergence
IMD	India Meteorological Department	TRMM	Tropical rainfall measuring mission
GPM	Global precipitation mission	HRLDAS	High resolution land data assimilation
MIL	Milbrandt scheme	NWP	Numerical weather prediction
TAA	Thompson aerosol aware scheme	DTC-UPP	Development testbed center unified post processor
		WRF-ARW	Advanced research WRF
		NOAA	National Oceanic and Atmospheric Administration
		NCEP	National Center for Environmental Prediction
		FSL	Forecast System Laboratory
		GDAS	Global data assimilation system
		NASA	National Aeronautics and Space Administration
		JAXA	Japan Aerospace Exploration Agency

Responsible Editor: C. Simmer.

✉ Sandeep Pattnaik  
spt@iitbbs.ac.in

<sup>1</sup> School of Earth, Ocean and Climate Sciences, Indian Institute of Technology Bhubaneswar, Argul, Jatni, Khurda, Odisha 752 050, India

<sup>2</sup> India Meteorological Department, Mausam Bhawan, Lodi Road, New Delhi 110 006, India

CC	Correlation coefficient
RMSE	Root mean square error
3AR	3 Day accumulated rainfall from 13 to 15th August
ETS	Equitable Threat Score
HSS	Heidke Skill Score
CRA	Contiguous rainfall area
MSE	Mean squared error
ECMWF	European Centre for Medium Range Weather Forecast
ERA5	ECMWF reanalysis 5th generation
DWR	Doppler weather RADAR
CFAD	Contour frequency altitude diagram
w.r.t.	With respect to
UGC	University Grants Commission
SERB	Science and Engineering Research Board

## 1 Introduction

In the month of August 2018, Kerala, a southern state in the west coast of India, witnessed extremely heavy rainfall. This event led to 42% above normal rainfall for the duration of 1–19 August (i.e., 2346.6 mm rainfall received against the normal of 1649.5 mm), and the maximum rainfall was experienced from 13 to 17 August over Kerala (India Meteorological Department (IMD) Report 2018). This Heavy Rainfall Event (HRE) resulted in massive floods, displacing more than a million people from their homes, damaging roads and bridges, causing about 480 deaths, and leading to an estimated loss worth approximately \$3 billion USD. The spatial distribution of district-wise rainfall shows that the highest excess rainfall occurred over Idukki (92% above normal) followed by Palakkad (72% above normal). These types of extreme weather events producing heavy rainfall and floods are the major natural hazards in many parts of the world, including India (Ahern et al. 2005). During the active monsoon phase, the movement of synoptic-scale systems many times causes HREs over the east and west coast of India and contributes substantially to Indian seasonal rainfall (Dodla and Ratna 2010; Pattanaik and Rajeevan 2009). Usually, orographic convection plays an important role in the occurrence of the HREs in the hilly areas of the west coast and parts of north-eastern India (Saha 1974; Vellore et al. 2014, 2016, 2019), leading to flash floods (Kumar et al. 2012). Accurate and quantitative forecasts of HRE (daily rainfall amounts  $\geq 120$  mm as per IMD) with adequate lead time over areas of a few thousand square kilometers are needed by disaster managers and administrators to minimize the loss of lives and properties (Hally et al. 2014).

### 1.1 Retrospective studies on HREs over the Indian region

In general, exclusively with reference to HRE, only a few studies have been carried out over the Indian region. In a recent study, Baisya and Pattnaik (2019) inferred that the HRE over Kerala in 2018 was caused by a continuous supply of moisture to the Western Ghats by an anomalous moisture channel along with the advection of moisture towards the southern peninsula by a monsoon depression. They also identified the presence of a positive quasi bi-weekly oscillation, along with an intra-seasonal oscillation over the region, to play an important role in the shedding of the towers of moisture flux convergence (MFC) by the depression. Another study by Viswanadhapalli et al. (2019) identified the strong westerly jet along with the formation of an offshore vortex, the transport of mid-tropospheric moisture under the presence of conducive vertical shear of horizontal wind, and the transport of mid-tropospheric moisture from the BOB to be the major factors responsible for the HRE of 2018 in Kerala. The sensitivity of CMP schemes for the HRE over Chennai in 2015 was investigated by Reshmi Mohan et al. (2018). Their results suggest that Thompson et al. (2008) and Morrison et al. (2005) schemes were able to identify features such as the location of maximum rainfall, its spatial distribution, and time of occurrence in close agreement with the observations by realistically predicting the high magnitude of vertical velocity associated with high instability, strong mid-level convergence and upper air divergence associated with strong cyclonic vorticity. Another study by Srinivas et al. (2018), identified that the veering wind with height associated with strong wind shear in the layer 800–400 hPa and the dry air advection are the main initiators of the development of instability and initiation of convection. Based on the results obtained from the simulation of the 2013 HRE in Uttarakhand with High-Resolution Land Data Assimilation (HRLDAS) modelling system, Rajesh et al. (2017) concluded that better representation of different land surface fields such as soil moisture, soil temperature etc. consequently leads to improved prediction of the anomalous extreme weather events over the Indian region. In another study, Agnihotri and Dimri (2015), using Weather Research and Forecasting (WRF) model simulations, found that the presence of a north–south trough, an easterly trough and low pressure areas over the surrounding Indian seas during the pre-monsoon season are the major precursors for the HREs caused by widespread thunderstorm activities over the southern peninsular India.

### 1.2 Studies of HREs in the global context

A study on the Sierra Nevada spillover precipitation of 1997 and 2006 by Kaplan et al. (2012) identified a mesoscale circulation with rising motion in the leeward side to be the

major factor for the HREs and concluded that the investigation of dynamical interactions on both synoptic and sub-synoptic scales is essential for better understanding of this kind of HREs. Numerical experiments carried out over the Red Sea by Dasari et al. (2014) indicated that the model-produced rainfall is strongly modulated by the choice of microphysical schemes, and it was noted that Lin and Thompson scheme produces the best result in that scenario. In another study, Ault et al. (2011) suggested that Asian dust may have an impact on atmospheric rivers and speculated that Thompson Aerosol Aware (TAA) scheme might simulate more accurate precipitation for simulations for HREs over the west coast of the United States of America. However, Tan (1997) found that TAA had less accuracy in the rainfall prediction than the Thompson scheme in the simulation of the California New Year's flood event in 1997.

### 1.3 Impacts of cloud microphysical parameterization

With the evolution of Numerical Weather Prediction (NWP) and Climate models, there has been immense progress in the understanding of cloud microphysical processes, and subsequently, many cloud microphysical parameterization (CMP) schemes have been developed. Water vapour, cloud droplets, cloud ice crystals, snow, rimed ice, graupel, and hail are the primary microphysical species whose budgets depend on the atmospheric dynamical and thermodynamical conditions which determine the partitioning of the hydrometeors themselves (Huang and Wang 2017). The NWP models predict rainfall using convective and microphysics parameterization for the representation of the clouds and precipitation processes (Powers et al. 2017). These parameterizations play an important role in prediction of the precipitation, hydrometeor distributions, and other associated variables. At higher resolution (1–3 km), precipitation can be explicitly resolved with better representation of mesoscale features through a cloud microphysics scheme without cumulus parameterization (Ghosh et al. 2016). In a CMP sensitivity study using the MM5 model, Grubišić et al. (2005) showed that the Resin2 mixed-phase scheme simulated the event with the highest accuracy among other schemes, and also the quantitative precipitation forecast skill was higher on the windward side than the leeward side of the mountain. Rajeevan et al. (2010) suggested that with an enhanced horizontal resolution of the models, the cloud microphysical processes play an important role by directly influencing the cold pool strength by modulating evaporation of rainfall and condensational heating in HREs over Southeast India. According to McCumber et al. (2010), the inclusion of mixed-ice phase cloud microphysics in the cloud model significantly contributes to the betterment of the output in convective simulations.

### 1.4 Importance of moisture flux convergence

In addition to cloud microphysical processes/parameters, synoptic scale features such as Moisture Flux Convergence (MFC) plays an important role in the evolution, sustenance of HREs. The prominent relationship between surface horizontal mass convergence and convective storms is well established (Breiland 1958; Matsumoto 1967; Peslen 1980) and many studies have quantified the role of surface horizontal mass convergence to storm initiation through real-time forecasting experiments and field projects (Wilson and Schreiber 1986; Wilson and Mueller 1993; Wilson and Megenhardt 1997).

### 1.5 Objective

This primary objective of this study is to investigate the effects of CMPs in the WRF model on the HRE of Kerala in August 2018. This study validates the model-simulated results, especially rainfall, with in-situ observations for better understanding of location-specific impacts of the HRE and also, quantifies the contributions of the different components of the Mean Squared Error (MSE), i.e., pattern, displacement, and volumetric error, over the study region by means of a spatial verification method, such as Contiguous Rain Area (CRA) (Ebert and McBride 2000). However, in the present study, not only the relative sensitivities of various CMPs are critically analyzed for the HRE of Kerala (2018) using the WRF model, but also the contribution and interactions of large scale factors such as MFC and orographic influence are investigated. The paper is organized in four sections. The experiment design is given in Sect. 2, followed by the discussion of results and conclusions in Sects. 3 and 4, respectively.

## 2 Model and data description

### 2.1 Experiment design

The simulations of the HRE of Kerala have been executed using the state-of-the-art Advanced Research Weather Research and Forecasting (WRF-ARW) Model version 3.9 (Skamarock et al. 2008) developed by the collaborative efforts of the National Center for Atmospheric Research (NCAR), National Oceanic and Atmospheric Administration (NOAA) [represented by National Center for Environmental Prediction (NCEP) and the (then) Forecast System Laboratory (FSL)], University of Oklahoma and other US Governmental agencies. It is a fully compressible, non-hydrostatic (with a run-time hydrostatic option) and a next-generation mesoscale numerical weather prediction model used for both research and operational forecasting purposes. The model

**Table 1** WRF-ARW model configuration

Model aspects	Settings
Version	3.9
Grid	Two grids, spatial resolutions are 9 and 3 km Vertical Grid: 35 levels (sigma coordinate)
Dynamics	Non-hydrostatic
Run period	96 h
Map projection	Mercator
Horizontal grid system	Arakawa C-Grid
Initial and lateral boundary conditions	0.25° × 0.25° 6-Hourly National Centre for Environmental Prediction (NCEP) GDAS/FNL Global Tropospheric Analyses ( <a href="https://rda.ucar.edu/datasets/ds083.3">https://rda.ucar.edu/datasets/ds083.3</a> )
Physics options	Parameterization schemes
PBL	MRF (Hong and Pan 2002) scheme
Radiation	Rapid Radiative Transfer Model (RRTM) longwave scheme for longwave radiation (Mlawer et al. 1997) Dudhia shortwave (Dudhia 1989) scheme for shortwave radiation
Surface scheme	Noah scheme (Niu et al. 2011) for land surface processes Monin–Obukhov Similarity scheme for surface heat and moisture fluxes (Monin and Obukhov 1954)
Cumulus parameterization	Kain-Fritsch (new eta) scheme (John 2004) used only in the outer domain with horizontal resolution of 9 km
Explicit microphysics	Milbrandt-Yau scheme (Milbrandt and Yau 2005) Aerosol Aware Thompson Scheme (Thompson and Eidhammer 2014) WRF Double Moment 6-class (WDM6) Scheme (Lim and Hong 2009) WRF Single Moment 6-class (WSM6) Scheme (Hong and Lim 2006)

was configured with two interactive nested domains with 35 vertical levels with the model top at 50 hPa. To incorporate the effects of boundary layer processes properly, high resolution (interval of 25 hPa) of vertical levels is employed between the surface (1000 hPa) to 850 hPa pressure level. The outer domain was configured with 9 km resolution, and the inner domain had a horizontal resolution of 3 km (Fig. 1). As the objective is to investigate the rainfall characteristics of 13–15 August, the simulations were initialized at 00 UTC 12 August 2018, and the model was integrated up to 96 h, i.e., till 00 UTC 16 August 2018. The initial and boundary conditions for the simulations were obtained from NCEP Global Data Assimilation System (GDAS)/Final (FNL) 0.25° × 0.25° Global Tropospheric Analyses (NCEP 2015), and the boundary conditions were updated every 6 h with the GDAS forecasts. Also, Real-Time Global (RTG) ([www.polar.ncep.noaa.gov](http://www.polar.ncep.noaa.gov)) data have been used to update the sea surface temperature (SST) every 6 h throughout the course of the simulation. The physics options included the RRTM scheme (Mlawer et al. 1997) for longwave radiation and Dudhia scheme (Dudhia 1989) for shortwave radiation, Noah scheme (Niu et al. 2011) for land surface processes, Monin–Obukhov Similarity scheme (Monin and Obukhov 1954) for surface heat and moisture fluxes, MRF scheme (Hong et al. 1996) for planetary boundary layer processes. The Kain-Fritsch (new eta) scheme (John 2004) was used for cumulus convection for the outer domain with 9 km resolution, and in the inner domain, only microphysical parameterization was used, but no cumulus convective

parameterization. Keeping other physics options same, four bulk CMP schemes, namely the WRF single-moment 6-class (WSM6) (Lim and Hong 2009), WRF double-moment 6-class (WDM6) (Hong et al. 2010), TAA scheme (Thompson and Eidhammer 2014), and Milbrandt (MIL) scheme (Milbrandt and Yau 2005) are considered (Table 1). The features and advantages of each of the CMP schemes taken into consideration for this study have been briefly discussed in Table 2. The model output is further post-processed with the Development Testbed Center Unified Post Processor (DTC-UPP) for analysis.

## 2.2 Descriptions of the datasets

- A. *ERA5* (Hersbach et al. 2018) The European Centre for Medium-Range Weather Forecast (ECMWF) Reanalysis 5th Generation dataset (ERA5) hourly data with a 0.25° spatial resolution has been used for hydrometeor validation. The values of the variables cloud liquid water; rain and ice have been employed for comparing the performance of the model. (url: <https://cds.climate.copernicus.eu/cdsapp#!/dataset/reanalysis-era5-pressure-levels>)
- B. *TRMM 3B42* (Huffman et al. 2007) The Tropical Rainfall Measuring Mission (TRMM) is a joint venture of the National Aeronautics and Space Administration (NASA) and Japan Aerospace Exploration Agency (JAXA) which provides 3 hourly gridded rainfall data (3B42). The TRMM 3B42 precipitation data of 3-h temporal resolution and 0.25° spatial resolution has been used to

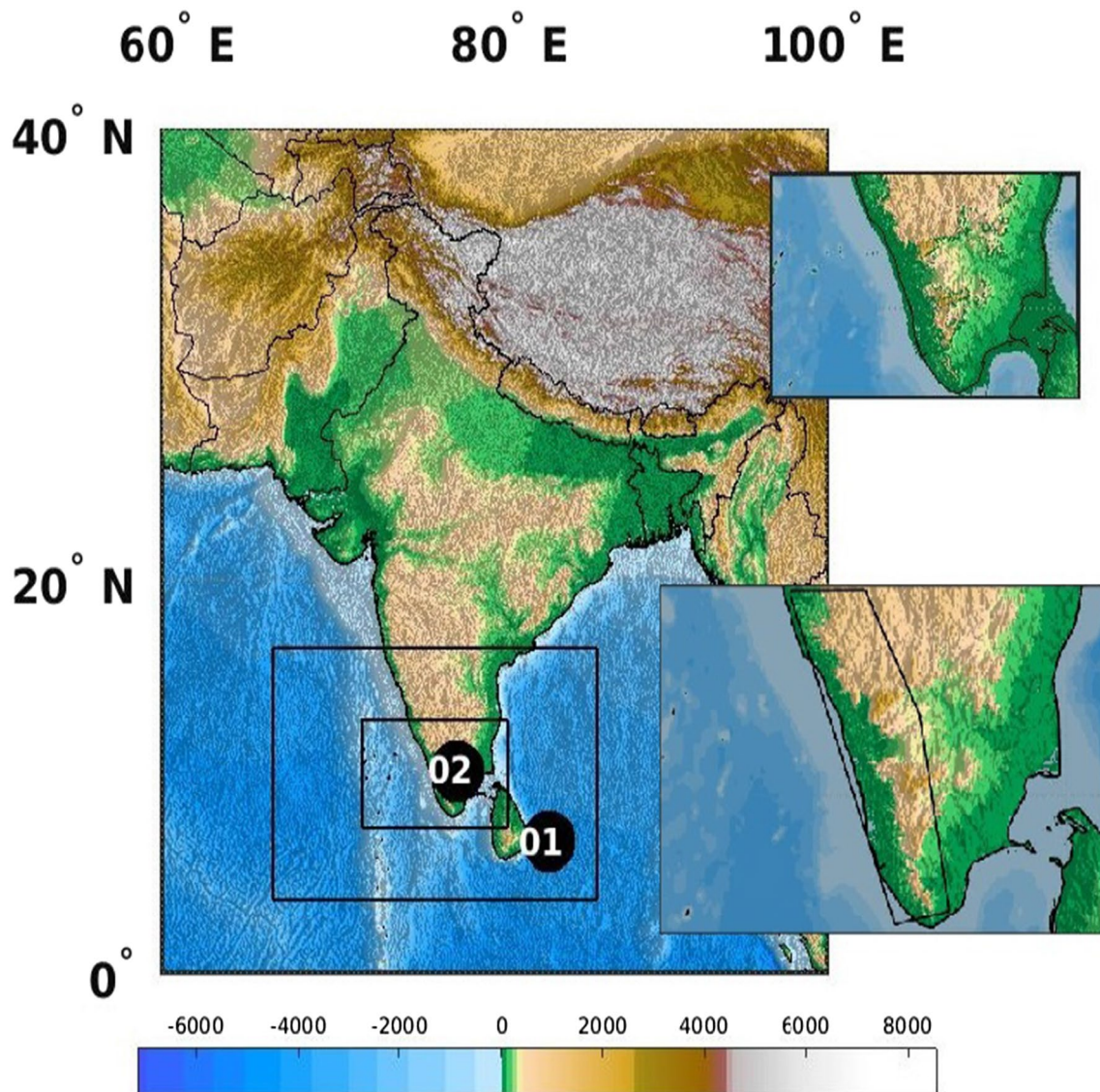


**Fig. 1** The domains selected for the simulation, the above offset indicates Domain 2 (inner domain) and the below offset indicates the analysis polygon in the inner domain. The elevation is given in m

find the peaks of rain rate, which were then compared to the peaks of moisture flux convergence produced by the model. (<https://gpm.nasa.gov/data-access/downloads/trmm>)

C. *GPM* (Huffman et al. 2014) The Global Precipitation Measurement (GPM) final run merged daily rainfall data with 1° spatial resolution has been used to validate the quantity and areal span of the daily accumulated rainfall as produced by the simulations. This dataset has also been used for calculating the Equitable Threat Score of rainfall as simulated by the model. This data was also used for CRA Analysis. (url: <https://gpm.nasa.gov/data-access/downloads/gpm>)

D. *IMD Station data* Data from India Meteorological Department (IMD) stations over Kerala are used for point validation of the model produced rainfall. Out of 88 stations, 31 stations are taken into consideration in this study.

### 3 Results and discussion

The model output analysis is carried out for the duration i.e. 12–15 August 2018 (day-1 to day-4 model forecasts). This section has been divided into six sub-sections illustrating the IMD station data validation, spatial distribution of rainfall predicted by different schemes and their comparison to

**Table 2** Table with the features and basic advantages of the CMPs used in this study

CMPs	Features	Advantages
Milbrandt (MIL) (Milbrandt and Yau 2005)	Double moment Uses gamma distribution function for particle size distribution Predicts 6 classes of hydrometeors (cloud water, rain, ice, snow, graupel and hail)	Can be used as a triple moment scheme by varying the shape parameter
Thompson Aerosol Aware (TAA) (Thompson and Eidhammer 2014)	Double moment Updated version of Thompson Microphysical scheme (Thompson et al. 2008) Predicts 5 classes of hydrometeors (cloud water, rain, ice, snow and hybrid graupel-hail)	Unlike the Thompson et al. (2008) CMP, this scheme can track and predict the number of available aerosols by nucleating water and ice from their dominant respective nuclei
WRF Double Moment 6-Class scheme (WDM6) (Lim and Hong 2009)	Double moment Updated from the WSM6 Predicts six classes of hydrometeors (water vapour, cloud water, rain, ice, snow and graupel)	Unlike WSM6, this scheme is incorporates the number concentration of cloud and rain water together with Cloud Condensation Nuclei (CCN). Simulates the warm-rain component better than its single moment counterpart (Zhang et al. 2018)
WRF Single Moment 6-Class Scheme (WSM6) (Hong and Lim 2006)	Single moment Updated version of WRF Single Moment 5-class Scheme (Lim and Hong 2005) Predicts six classes of hydrometeors (water vapour, cloud water, rain, ice, snow and graupel)	WSM6 incorporates the graupel processes for better microphysical investigation than WSM5 scheme. Performs better in light precipitation scenarios (Lim and Hong 2005)

the Global Precipitation Measurement (GPM) observations and the CRA analysis, reflectivity and hydrometeor analysis using Contour Frequency Altitude Diagram (CFAD), analysis of vertical velocity and temperature profiles, analysis of the contributions of the different terms of the moisture budget equation and the influence of orography, respectively.

### 3.1 Station validation

Based on the threshold amount of rainfall (3 days accumulated rainfall > 100 mm), model-derived 24 h rainfall is validated against 31 IMD stations (out of 87) for day-2 to day-4 forecasts. In addition, model-simulated three days accumulated rainfall is also validated against IMD station observations. Furthermore, the maximum rainfall was observed in the districts of Idukki and Palakkad (IMD Report 2018). Therefore, 4 stations from the district of Idukki, viz., Idukki, Thodupuzha, Munnar and Peermade, and 3 stations from the district of Palakkad, viz., Alathur, Parumbikulam, and Pattembi are considered for validation among these 31 stations. The IMD stations in the state of Kerala are shown in Fig. 2.

To investigate and analyze the error of the model simulated rainfall with IMD station observations, the Taylor diagram (Taylor 2001) is prepared (Fig. 3). In this diagram, the radial distance from the origin gives the value of standard deviation and the azimuthal position of model computed rainfall gives the correlation coefficient (CC). Also, the distance between the observation and the model computed rainfall gives the root mean square error (RMSE). It is evident from Fig. 3 WDM6 (Fig. 3c) simulated the rainfall with minimal RMSE and maximum CC for the maximum number of stations, followed by WSM6 (Fig. 3d).

The day-wise rainfall from day-2 to day-4 and also the 3 days accumulated rainfall from 13 to 15th August (3AR), as predicted by WDM6 with the 31 IMD station observations are given in Table 3 (the tables for MIL, TAA and WSM6 are not given). All the schemes overestimated the rainfall at most of the stations (Trivandram Aero, Aryankavu, Alathur, Chengannur, Haripad, etc.) on day-3 (14 August 2018), i.e., the day of maximum rainfall. But the 3AR was underestimated at some of the stations (Irikkur, Idukki, Kochi, Kannur, Quilandi, Kodungallur, Vadakkancherry, Vallanikkara etc.). In general, it is noted that model experiments were able to better capture the rainfall at day-3 compared to day-4. The increase in errors for day-4 (leading to an increase in 3AR forecast errors) is due to the underestimation in the rainfall forecast. For specific discussion, three stations are chosen based on their geographical locations in the Kerala state i.e., Kannur (North), Kochi (Central), and Thiruvananthapuram (South) (see Fig. 2 for specific locations of the stations). At Kannur, all the schemes have underestimated the 3AR compared to IMD. However, over the same location, day-3 (24 h accumulated) rainfall was well forecasted by the different



**Fig. 2** IMD stations situated in Kerala. Source: Daily Weather Report, IMD Thiruvananthapuram. [https://www.imdtvm.gov.in/index.php?option=com\\_content&task=view&id=21&Itemid=35](https://www.imdtvm.gov.in/index.php?option=com_content&task=view&id=21&Itemid=35)

schemes considered in this study, but with an underestimation tendency in magnitude as compared to observations. The differences were within the range of 14–30 mm, with the highest (lowest) values 29.13 mm (14.105 mm) is noted for WDM6 (WSM6). Similarly, at Kochi, huge underestimation ( $> 150$  mm) of 3AR is noted for all schemes with TAA and MIL predicting the least amount of rainfalls with the magnitude of differences of 177.47 mm and 166.3 mm, respectively. For the same station, the least errors are noted for WDM6 (WSM6) with 76.415 mm (95.415 mm). However, a completely different picture was seen at Thiruvananthapuram, where all the schemes except MIL underestimated the 3AR (difference of 31.24 mm). But for day-3, all the schemes overestimated the rainfall, with WDM6 producing the least error (5.655 mm) and TAA having the largest error (61.465 mm). In the district of Idukki, where the heaviest rainfall was observed, at the stations Idukki and Peermade, the 3AR was underestimated by all the schemes with MIL

and TAA showing the largest error. But on day-3, all the schemes forecasted the rainfall close to that of IMD. WDM6 yielded the best performance with the estimation of day-3 and day-4 rainfall differences to be the least by only 1.685 and 5.805 mm, respectively, at Munnar. TAA produced a large error in this district. Again, in the district of Palakkad (second highest rainfall), 3AR was best predicted by WDM6 and worst by the TAA. Furthermore, WDM6 again produced the least 3AR error differences ( $< 50$  mm) for stations such as Parumbikulam, Pattermbi (Palakkad district) (Table 3). In general, it is noted that 3AR was best predicted by WDM6 consistently with the least errors ( $< 100$  mm) at 22 stations followed by WSM6 with the least errors ( $< 100$  mm) at 16 stations. The MIL and TAA are the worst-performing schemes with 11 stations having differences more than 150 mm. The percentage error in the prediction of 3AR for all the schemes is shown in Table 4. It is seen from Table 4 that out of the 31 stations taken into consideration, the 3AR

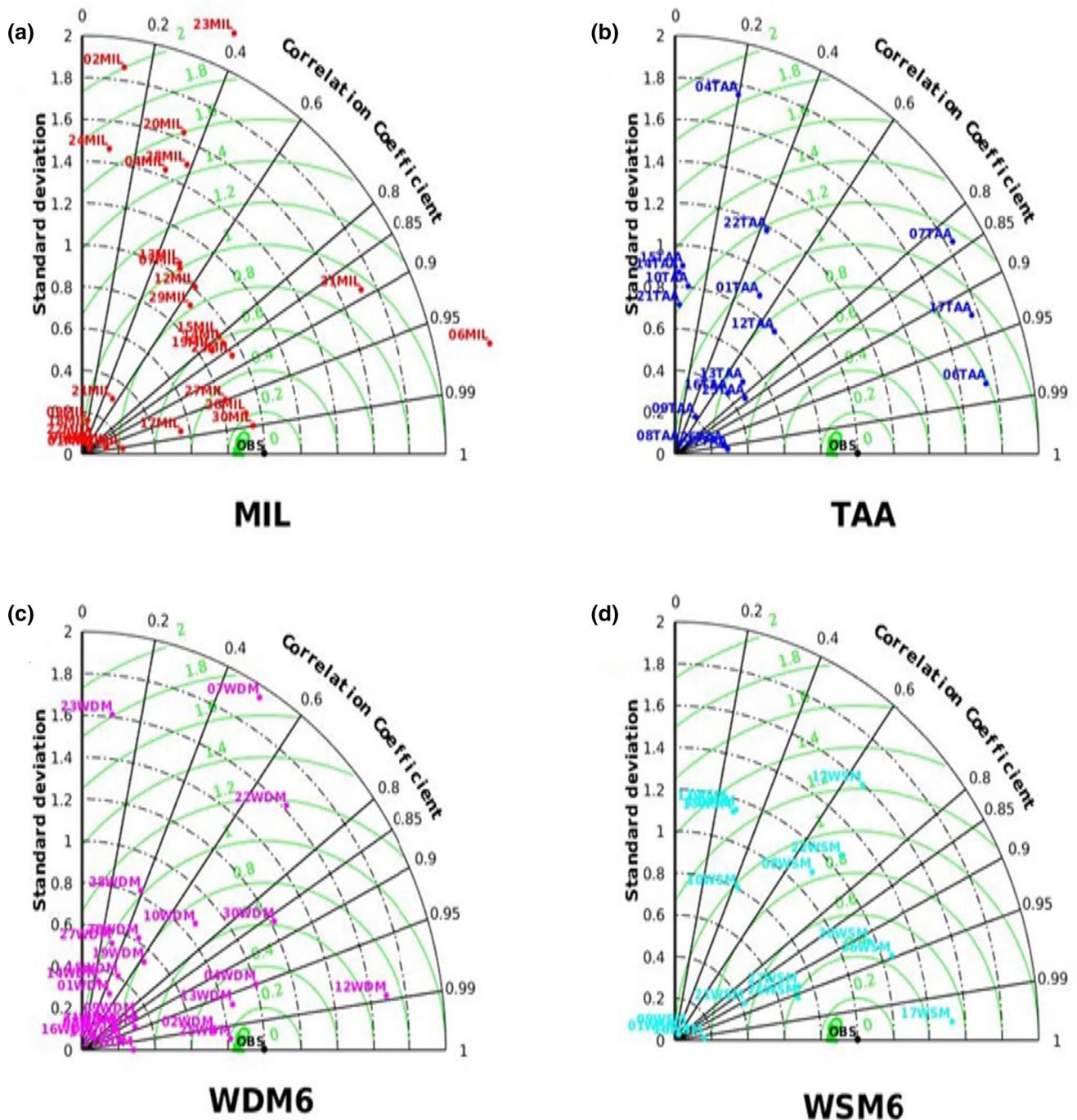


**Fig. 3** a–d Taylor Diagram for station data validation (31 stations chosen on the basis of  $3AR > 100$ ) for all the schemes with respect to IMD stations for 3AR

was predicted with less than 25% error by WDM6 at 12 stations (highest) and TAA at 5 stations (lowest).

### 3.2 Rainfall

Figure 4a–t shows the spatial distribution of cumulative rainfall received on all the days from model experiments

and observation (GPM). As there are no rainfall datasets available at a high resolution of 3 km (model resolution), the GPM Final Run dataset, which has a spatial resolution of 25 km, is used for spatial rainfall validation. Therefore, the GPM dataset is remapped (rainfall is conserved in the remapping) to the model grid resolution for validating the model-produced rainfall with the aim to capture



**Table 3** The day wise account of the accumulated rainfall (day-2, 3, and 4) as predicted by WDM6 along with the IMD observations (31 stations over Kerala)

Station name	Latitude	Longitude	Day 2 (13th August 2018)			Day 3 (14th August 2018)			Day 4 (15th August 2018)			Total accumulated (72 h)		
			IMD	WDM6	Diff	IMD	WDM6	Diff	IMD	WDM6	Diff	IMD	WDM6	Diff
Irikkur	11.97° N	75.55° E	48.0	0	48.0	54.0	43.778	10.222	178.0	4.085	173.915	280.0	47.863	232.137
Kochi	10.15° N	76.40° E	14.3	0.03	14.27	8.1	63.388	-55.288	171.9	54.495	117.405	194.3	117.885	76.415
Idukki	9.83° N	76.92° E	72.0	0	72.0	82.0	110.41	-28.41	235.0	60.440	174.56	389.0	170.85	218.15
Thodupuzha	9.83° N	76.67° E	26.5	0	26.5	15.8	91.032	-75.232	168.0	46.130	121.87	210.3	137.163	73.137
Munnar	10.00° N	77.15° E	113.8	21.235	92.56	117.5	119.185	-1.685	216.0	221.805	-5.805	447.3	362.225	-85.075
Peermade	9.57° N	76.98° E	58.0	0	58.0	93.0	51.505	41.495	274.0	72.81	201.19	425.0	124.315	300.685
Aryankavu	8.98° N	77.17° E	34.0	11.46	22.54	24.0	64.89	-44.89	168.0	136.56	31.44	226.0	212.91	13.09
Kozhikode	11.25° N	75.78° E	34.4	4.46	29.94	86.0	9.318	76.682	197.2	7.43	189.77	317.6	21.208	296.392
Karipur AP	11.13° N	75.95° E	50.4	0.02	50.38	90.3	18.82	71.48	210.2	7.80	202.4	350.9	26.64	324.26
Manjeri	11.12° N	76.12° E	42.0	13.95	28.05	84.0	60.948	23.052	200.0	63.26	136.74	326.0	74.905	251.095
Alathur	10.63° N	76.63° E	26.5	2.01	24.49	24.6	46.775	-22.175	177.5	30.79	146.71	228.6	79.575	-149.025
Chengannur	9.32° N	76.62° E	16.0	0.0	16.00	6.0	53.915	-47.915	110.0	79.78	30.22	132.0	133.695	-1.695
Haripad	9.28° N	76.45° E	0.0	0.0	0.0	5.2	36.093	-30.893	124.2	48.40	75.8	129.4	84.493	44.907
Kayamkulam	9.18° N	76.50° E	10.4	0.0	10.4	5.0	94.245	-89.245	123.0	49.06	73.94	138.4	143.305	-4.905
Kayamkulam_Agri	9.17° N	76.52° E	11.1	0.0	11.1	4.3	98.465	-94.165	114.1	50.51	63.59	129.5	148.975	-19.475
Kannur	11.87° N	75.37° E	75.5	3.05	72.45	29.8	0.67	29.13	136.8	27.02	109.78	242.1	30.745	211.355
Taliparamba	12.05° N	76.35° E	44.8	0.0	44.8	16.6	36.67	-20.07	137.4	54.53	82.87	198.8	91.2	107.6
Alwaye PWD	10.12° N	76.35° E	10.0	3.23	6.77	6.4	65.443	-59.043	138.0	48.115	89.885	154.4	116.788	37.612
Ernakulam South	9.97° N	76.28° E	18.0	0.43	17.57	6.0	23.870	-17.87	111.0	47.72	63.28	135.0	72.02	62.98
Kumarakam	9.62° N	76.43° E	0.0	1.55	-1.55	11.2	65.995	-54.795	92.0	72.95	19.05	103.2	140.495	-37.295
Quilandi	11.45° N	75.70° E	60.0	5.25	54.75	67.0	48.53	18.47	153.0	32.48	120.52	280.0	86.26	193.74
Perinthalamanna	10.97° N	76.23° E	56.0	39.6	16.4	77.0	78.005	-1.005	145.0	98.16	46.84	278.0	215.76	62.24
Parumbikulam	10.33° N	76.75° E	34.0	34.37	-0.37	40.0	126.078	-86.078	145.0	106.92	38.08	219.0	267.37	-48.37
Pattambi	10.8° N	76.20° E	17.7	3.44	14.26	11.4	72.335	-60.935	116.2	38.77	77.43	145.3	114.54	30.76
Kurudamannil	9.35° N	76.74° E	12.8	0.07	12.73	16.6	45.580	-28.98	122.2	77.08	45.12	151.6	122.73	28.87
Thiruvanthapuram	8.47° N	76.95° E	20.5	22.32	-1.82	23.0	28.655	-5.655	138.6	58.01	80.59	182.1	108.985	73.115
Trivandram_Aero	8.48° N	76.92° E	12.0	23.05	-11.05	1.0	23.305	-22.305	125.0	60.31	64.69	138.0	106.665	31.335
Kodungallur	10.32° N	76.20° E	6.5	11.52	-5.02	3.0	44.8200	-41.82	136.0	24	112.0	145.5	80.34	65.16
Vadakkancherry	10.66° N	76.24° E	14.4	3.78	10.62	6.0	37.663	-31.663	153.4	35.89	117.51	173.8	77.335	96.465
Vallamkkara	10.5° N	76.28° E	26.5	0.085	26.415	8.3	31.175	-22.875	140.6	55.0	85.6	175.4	86.26	89.14
Manantoddy	11.8° N	76.02° E	78.0	51.415	26.585	96.0	117.795	-21.795	161.0	168.29	-7.29	335.0	337.5	-2.5

The differences are also shown (+ve and -ve differences indicate underestimation and overestimation by WDM6, respectively)

**Table 4** Percentage error of model-produced 3AR with respect to the IMD observations at the different stations (+ve and -ve error signifies overestimation and underestimation of rainfall by the model, respectively)

Station name	Latitude	Longitude	MIL			TAA			WDM6			WSM6		
			Obs	Model	% Error	Obs	Model	% Error	Obs	Model	% Error	Obs	Model	% Error
Irikkur	11.97° N	75.55° E	280	8.643	-96.91	280	22.763	-91.87	280	47.863	-82.91	280	3.533	-98.74
Kochi	10.15° N	76.40° E	194.3	27.998	-85.59	194.3	16.83	-91.34	194.3	117.885	-39.33	194.3	98.605	-49.25
Idukki	9.83° N	76.92° E	389	143.165	-63.197	389	62.445	-83.95	389	170.85	-56.08	389	235.845	-39.37
Thodupuzha	9.83° N	76.67° E	210.3	130.125	-38.12	210.3	67.388	-67.96	210.3	137.163	-34.78	210.3	247.86	17.86
Munnar	10.00° N	77.15° E	447.3	331.21	-25.95	447.3	283.663	-36.58	447.3	362.225	-19.02	447.3	347.94	-22.21
Peermade	9.57° N	76.98° E	425	162.55	-61.75	425	172.668	-59.37	425	124.315	-70.75	425	265.798	-37.46
Aryankavu	8.98° N	77.17° E	226	184.51	-18.35	226	289.3	28.01	226	212.91	-5.79	226	325.49	44.02
Kozhikode	11.25° N	75.78° E	317.6	9.395	-97.04	317.6	19.938	-93.72	317.6	21.208	-93.32	317.6	108.098	-65.96
Karipur	11.13° N	75.95° E	350.9	18.35	-94.77	350.9	35.74	-89.81	350.9	26.64	-92.41	350.9	26.19	-92.54
Manjeri	11.12° N	76.12° E	326	66.06	-79.73	326	131.55	-59.65	326	74.905	-77.02	326	144.38	-55.71
Alathur	10.63° N	76.63° E	228.6	90.76	-60.3	228.6	91.64	-59.91	228.6	79.575	-65.19	228.6	116.095	-49.21
Chengannur	9.32° N	76.62° E	132	173.65	31.55	132	185.735	40.71	132	133.695	1.28	132	275.17	108.46
Haripad	9.28° N	76.45° E	129.4	181.795	40.49	129.4	111.6	-13.76	129.4	84.493	-34.7	129.4	190.983	47.59
Kayamkulam	9.18° N	76.50° E	138.4	154.745	11.81	138.4	80.43	-41.89	138.4	143.305	3.54	138.4	155.57	12.41
Kayamkulam_Agri	9.17° N	76.52° E	129.5	158.565	22.44	129.5	95.84	-25.99	129.5	148.975	15.04	129.5	158.415	22.3
Kannur	11.87° N	75.37° E	242.1	33.96	-85.97	242.1	77.525	-67.98	242.1	30.745	-87.3	242.1	52.11	-78.48
Taliparamba	12.05° N	76.35° E	198.8	47.475	-76.11	198.8	50.44	-74.63	198.8	91.2	-54.12	198.8	87.655	-55.91
Alwaye PWD	10.12° N	76.35° E	154.4	35.833	-76.79	154.4	33.943	-78.02	154.4	116.788	-24.36	154.4	74.91	-51.48
Ernakulam South	9.97° N	76.28° E	135	30.37	-77.50	135	30.14	-77.67	135	72.02	-46.65	135	104.55	-22.56
Kumarakam	9.62° N	76.43° E	103.2	97.605	-5.42	103.2	16.03	-84.47	103.2	140.495	36.14	103.2	157.6	52.71
Quilandi	11.45° N	75.70° E	280	46.89	-83.25	280	58.72	-79.03	280	86.26	-69.19	280	54.09	-80.68
Perinthalamanna	10.97° N	76.23° E	278	80.655	-70.98	278	179.44	-35.45	278	215.76	-22.39	278	155.52	-44.058
Parumbikulam	10.33° N	76.75° E	219	178.978	-18.27	219	179.935	-17.84	219	267.37	22.09	219	339.503	55.02
Pattambi	10.8° N	76.20° E	145.3	28.775	-80.2	145.3	103.055	-29.07	145.3	114.54	-21.17	145.3	159.75	9.94
Kurudamannil	9.35° N	76.74° E	151.6	241.11	59.04	151.6	152.28	0.45	151.6	122.73	-19.04	151.6	285.94	88.61
Thiruvananthapuram	8.47° N	76.95° E	182.1	213.3475	17.15	182.1	180	-1.15	182.1	108.985	-40.15	182.1	155.09	-14.83
Trivandram_Aero	8.48° N	76.92° E	138	197.24	42.92	138	155.835	12.92	138	106.665	-22.71	138	163.21	18.27
Kodungallur	10.32° N	76.20° E	145.5	26.33	-81.90	145.5	12.29	-91.55	145.5	80.34	-44.78	145.5	32.21	-77.86
Vadakkancherry	10.66° N	76.24° E	173.8	28.383	-83.66	173.8	52.905	-69.56	173.8	77.335	-55.50	173.8	107.843	-37.95
Vallamikkara	10.5° N	76.28° E	175.4	32.715	-81.34	175.4	55.535	-68.34	175.4	86.26	-50.82	175.4	88.87	-49.33
Manantoddy	11.8° N	76.02° E	335	285.695	-14.72	335	170.995	-48.96	335	337.5	0.75	335	378.8	13.07

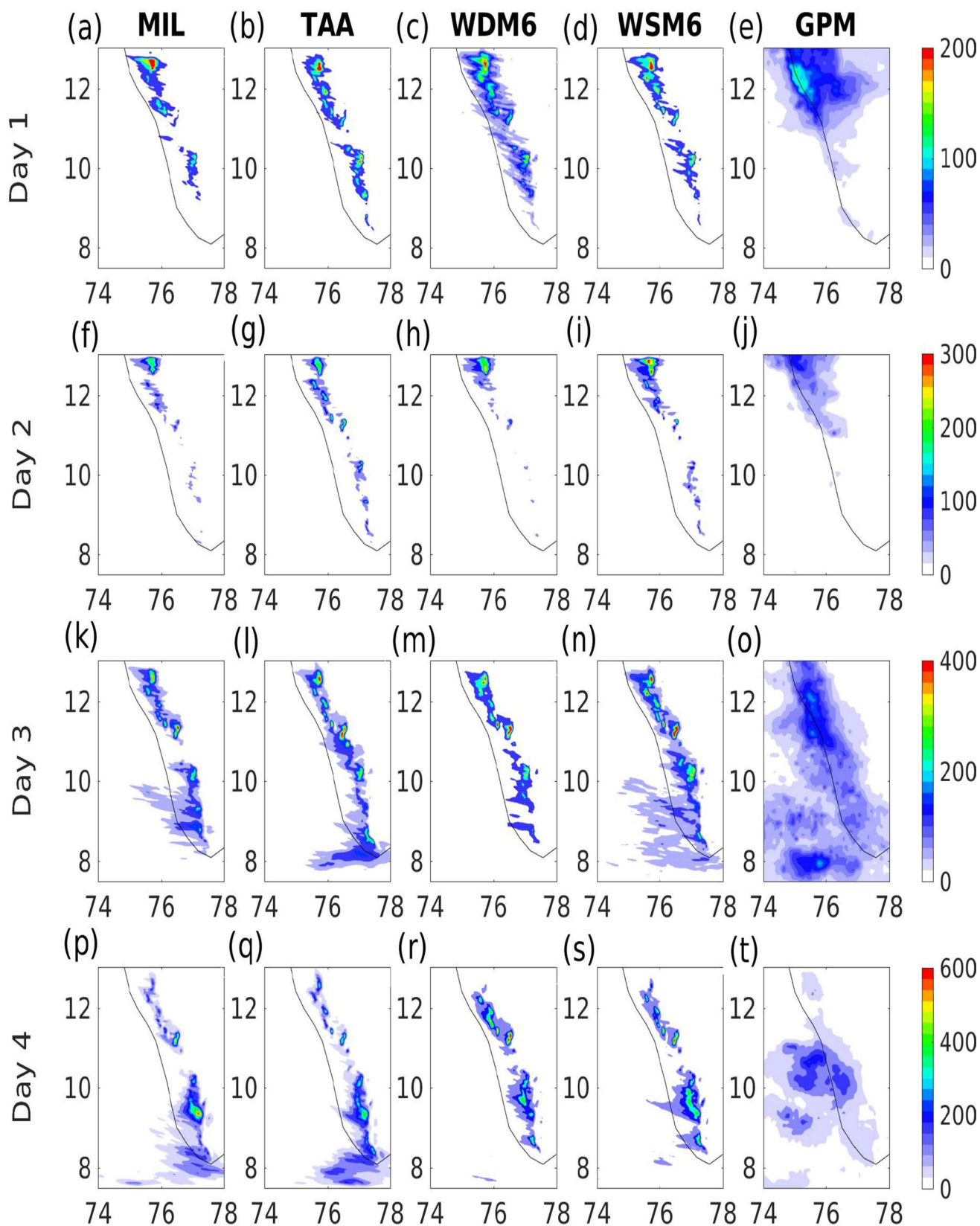


Fig. 4 a–t Daily accumulated rainfall (mm) for all the schemes for day-1 to day-4

the signatures of finer scale variabilities of rainfall seen at model resolution. Though the spatial extent of rainfall from north to south Kerala was captured by all the CMP schemes, the intense rainfall pockets were captured at different locations by the different CMP schemes. WDM6 and WSM6 are able to locate the pocket of intense rainfall zones in agreement with the observations on day-3 and day-4 (Fig. 4m and n). On day-3 and day-4, both the MIL (Fig. 4k and p) and TAA (Fig. 4l and q) have shown the rain systems to be dominant in the southern portion of Kerala more than the northern part, which does not agree with the GPM (Fig. 4o and t). WSM6 was able to capture the spread of rainfall over the adjacent coastal seas better than the other CMP schemes on day-3 (Fig. 4n). This finding is in agreement with the study over the East China Sea by Hong et al. (2010). Though WDM6 has predicted heavy rainfall over the land area splendidly on both day-3 and day-4, it was unable to capture the rainfall over the adjacent sea.

The zone of heavy rainfall over the state of Kerala is identified from Fig. 4. Hence, a polygon (shown in Fig. 1) over the desired area has been taken and further analyses of Equitable Threat Score (ETS) and Heidke Skill Score (HSS), hydrometeors, reflectivity, vertical velocity, latent heat, and moisture convergence have been carried out by masking the grid-points not belonging to this polygon, over the whole domain. This polygon will be termed as the analysis polygon from now on.

ETS and HSS are useful for categorical statistical validation of rainfall (Wilks 2011). To assess the performances of CMP experiments, the ETS and HSS have been calculated for all the four days (Fig. 5) over the analysis polygon. WSM6 shows the highest skill on day-1 (Fig. 5e). On day-2, the skills shown by WSM6 and WDM6 both are considerable (Fig. 5f). WDM6 shows the highest skills (both ETS and HSS) on day-3 and day-4 for almost all the thresholds of rainfall (Fig. 5g and h). MIL and TAA have consistently had poor skill scores (i.e., ETS and HSS) throughout the forecast duration. The same pattern of scores is also noted for HSS as well (Fig. 5a–d).

### 3.2.1 Contiguous Rain Area (CRA) Analysis

The main objective of the CRA method is to evaluate systematic errors in the prediction of rain systems (Ebert and McBride 2000; Grams et al. 2006). In this spatial verification method, the forecast and observational fields are matched to be on the same spatial grid. They are merged by overlaying the forecast on the observations and taking the maximum value at each grid point (Ebert and Gallus 2009). Thus forecast and observed entities overlapping with each other can now be taken into account in a

quantitative perspective in the merged field. After this, by setting up some minimum intensity threshold, an entity finder is applied to isolate distinct CRAs in the merged field.

The mean squared error (MSE) of the original forecast is decomposed in to the displacement (location), volume, and pattern error components as the following:

$$\text{MSE}_{\text{total}} = \text{MSE}_{\text{displacement}} + \text{MSE}_{\text{pattern}} + \text{MSE}_{\text{volume}} \quad (1)$$

The original decomposition, used with the minimum squared error best-fit criterion, computes the location component as the difference in the mean squared error before and after shifting the forecast, the volume error as the bias in mean intensity, and the pattern error as a residual:

$$\text{MSE}_{\text{displacement}} = \text{MSE}_{\text{total}} - \text{MSE}_{\text{shifted}} \quad (1a)$$

$$\text{MSE}_{\text{volume}} = (\bar{F} - \bar{X})^2 \quad (1b)$$

$$\text{MSE}_{\text{pattern}} = \text{MSE}_{\text{shifted}} - \text{MSE}_{\text{volume}} \quad (1c)$$

where  $\bar{F}$  and  $\bar{X}$  are the mean forecast and observed values after the shift.

The CRA analysis has been carried out for 72 h (day-2 to day-4 of forecast hours) with the model data generated by the four CMP schemes, and for observations, GPM has been considered. The threshold for the analysis has been taken as 150 mm as the rainfall event considered for this study was an HRE. The total error has been decomposed into three components, viz. displacement error, pattern error, and volume error. The number of grid points having 150 mm or more rainfall was identified differently by the different schemes. According to the GPM observations, 710 points had 150 mm or more rainfall, and the maximum number of grid points with this criterion was identified by the WSM6 (5513), followed by TAA (5213), WDM6 (4405), and MIL (2556). The magnitude of mean (maximum) rainfall in the grid points were underestimated (overestimated) by all the schemes. These results indicate that maximum rainfall zones have less spread characteristics across these experiments.

In Table 5, we can see that MIL captured two features of rainfall. The displacements of the features were slightly to the northeast and north for the two features, respectively, compared to that of the GPM. The first feature exhibited higher displacement error and lower volume error than the second feature, and the pattern error is similar for both these features. At the same time, all the other schemes are able to capture only one CRA. TAA showed second-highest amount of Mean Square Error (MSE). The CRAs captured by the TAA and WSM6 (Fig. 6b and d) have similar characteristics to another small feature detected by the GPM observations

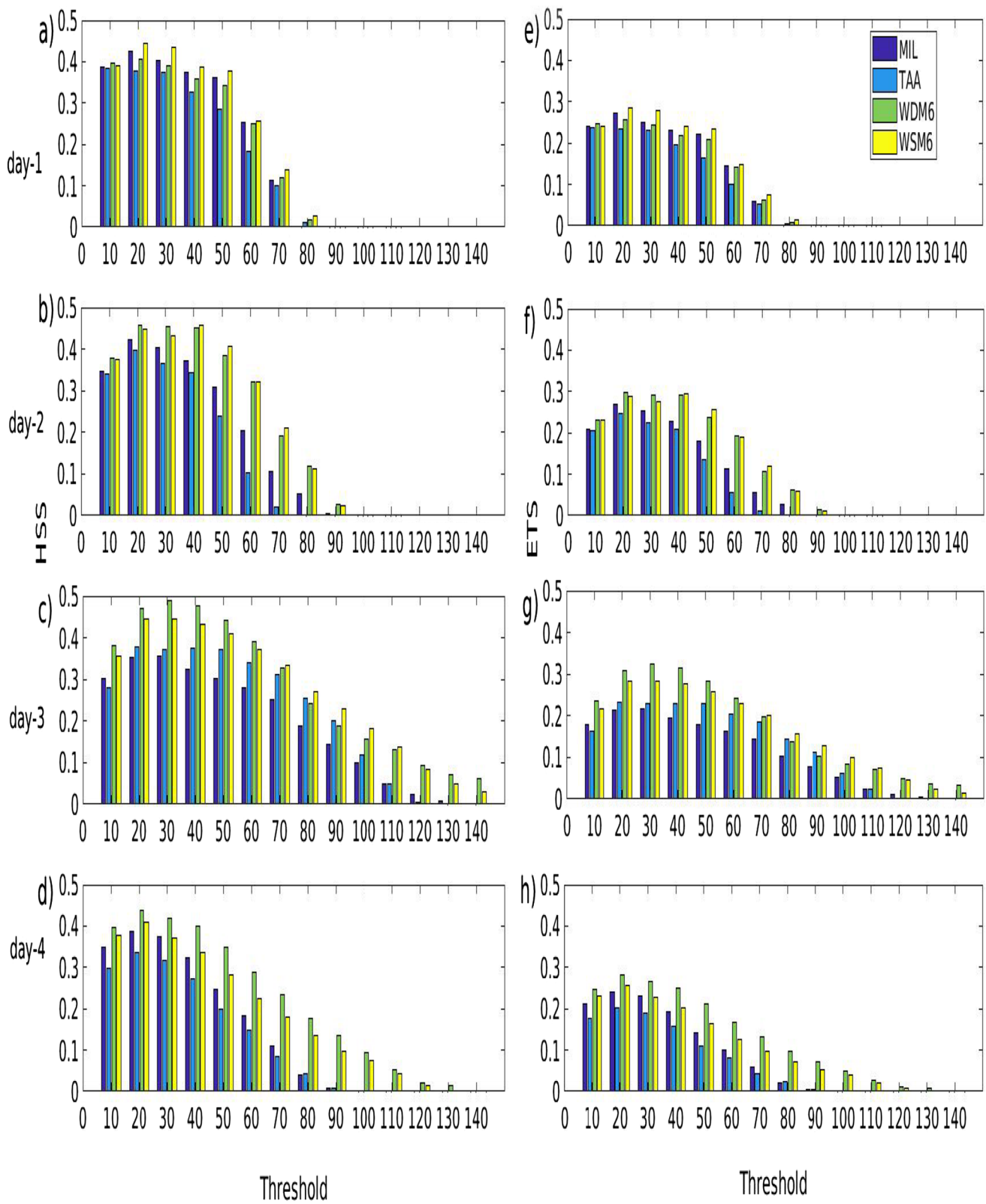


**Fig. 5** Day-wise HSS (a–d) and ETS (e–h) of rainfall of CMPs in comparison with GPM, calculated over the analysis polygon (Fig. 1)

**Table 5** Error decomposition for the CRAs for all the CMP schemes

Schemes	Features	Displacement (E,N)	Total MSE (mm)	Decomposed (%)
Milbrandt (MIL)	Feature 1	−0.023 E, 0.876 N	3258.359	Displacement error = 10.08 Pattern error = 87.64 Volume error = 2.28
	Feature2	0.851 E, −0.389 N	6391.654	Displacement error = 0.03 Pattern error = 88.95 Volume error = 11.02
Thompson Aerosol Aware (TAA)	Feature 1	1.121 E, 2.2815 N	9121.93	Displacement error = 42.43 Pattern error = 56.07 Volume error = 1.51
WDM6	Feature 1	0.446 E, −0.284 N	8310.994	Displacement error = 39.27 Pattern error = 60.4 Volume error = 0.32
WSM6	Feature 1	0.986 E, 2.714 N	11,577.41	Displacement error = 41.96 Pattern error = 56.39 Volume error = 1.64

just north of 12° N, but they could not capture the actual feature in accordance with the major feature identified by GPM. WSM6 showed the highest amount of error among the four schemes. The feature identified by WDM6 was the closest to the dominant feature identified (marked green in Fig. 6c) by the GPM (marked green in Fig. 6e) and had the least volumetric error. However, both the features identified by MIL have a huge pattern error. In the aspect of location features, MIL identified a better CRA, but volumetrically, WDM6 was the best scheme in determining the CRA. It is also to be noted that the GPM identified three features, but the third feature (indicated by yellow in the plot) could not be identified by any of the CMP schemes (Fig. 6e). In all the cases, pattern error appeared to be the major contributor to the total MSE which in accordance with the findings of Chen et al. (2018).

### 3.3 Hydrometeors and reflectivity

The time series of spatially averaged cloud ice, cloud liquid water, and rainwater for day-2 to day-4 over the analysis polygon (Fig. 1) for all the CMP schemes are shown in Fig. 7. For validation, the results obtained from the simulations with the four different CMP schemes are compared with the European Centre for Medium-Range Weather Forecast (ECMWF) Reanalysis 5th Generation (ERA5) data. It is evident that both MIL and TAA are not able to capture the evolution of the cloud ice at higher levels, but MIL captured the cloud ice better than the TAA with the maximum value of  $6 \times 10^{-6} \text{ kg kg}^{-1}$  at 200 hPa level on the beginning of day-4. The lack of cloud ice in the case of the MIL in spite of the prominent presence of cloud liquid water till higher levels might be justified by the presence of supercooled water in the mid-levels. Both the WDM6 and WSM6 were able to capture the evolution of the cloud ice from day-2 and show a similar structure of cloud ice with a maximum value

of  $40 \times 10^{-6} \text{ kg kg}^{-1}$  at 300–400 hPa level from halfway of day-3 (Fig. 7c and d). The most important thing is that these two schemes were able to predict the high concentration of the ice particles up to the middle troposphere. This pattern is in agreement with ERA5, where the upper-level cloud ice is prominent, and the extent of the cloud ice content is up to the middle atmosphere where the contours of the cloud ice overlap the contours of the cloud liquid water (Fig. 7e). The closely packed contours of cloud liquid water ranging from 15 to  $60 \times 10^{-6} \text{ kg kg}^{-1}$  as shown by the ERA5, were also found in the WDM6 and WSM6. The cloud liquid water and cloud ice content distribution is also similarly predicted by the WDM6 and WSM6. The WDM6 shows the highest peak of rainwater on day-3, which is well captured in terms of maximum rainfall simulated by the model. Thereafter, the magnitudes of rainwater decrease but remain significant till the end of day-4. This suggests that a better representation of liquid hydrometeors is noted in WDM6 with respect to the other schemes. This is to mention that rainwater was not at all captured by the MIL (Fig. 7a). Furthermore, WSM6 and TAA have shown a massive decrease in rainwater content on day-4, which does not agree with the ERA5. On day-4, the maximum rainwater content was shown by ERA5 (Fig. 7e), which is not shown by any of the schemes; however, WDM6 shows the nearest values on day 4 compared to the others. The model-simulated cloud snow and graupel distribution are also compared with ERA5 data. As the graupel data is not available from ERA5, only the cloud snow distribution is taken into account for ERA5. It is seen that WDM6 and WSM6 simulated almost similar cloud snow and graupel structure, whereas TAA and MIL were unable to predict these frozen hydrometeors to that extent. MIL showed a little amount of graupel in the higher levels, though the amount was considerably less than that of WDM6 and WSM6. This, along with the lack of cloud ice simulated by MIL, suggests that the generation of graupel is attributed to the riming of

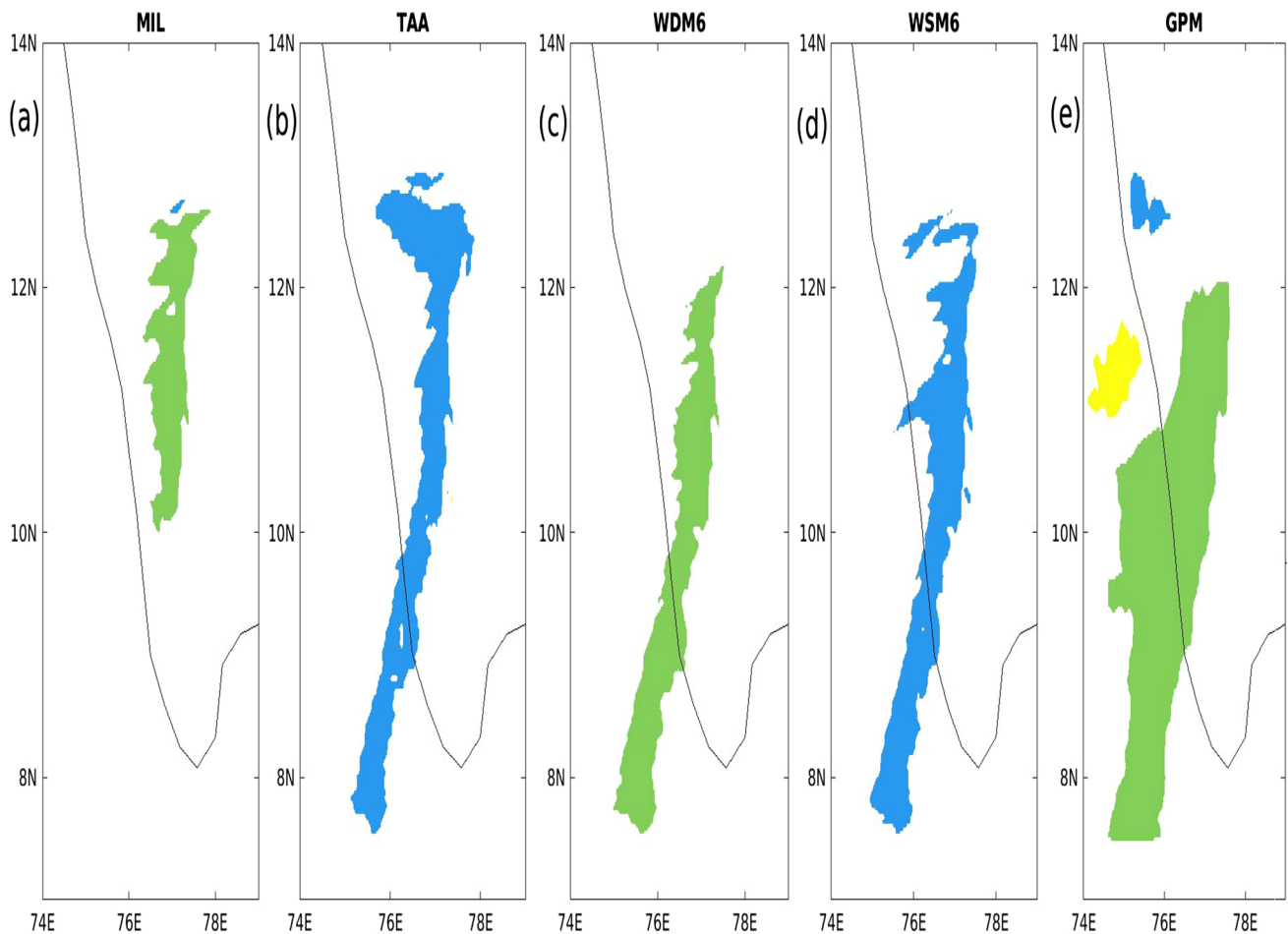


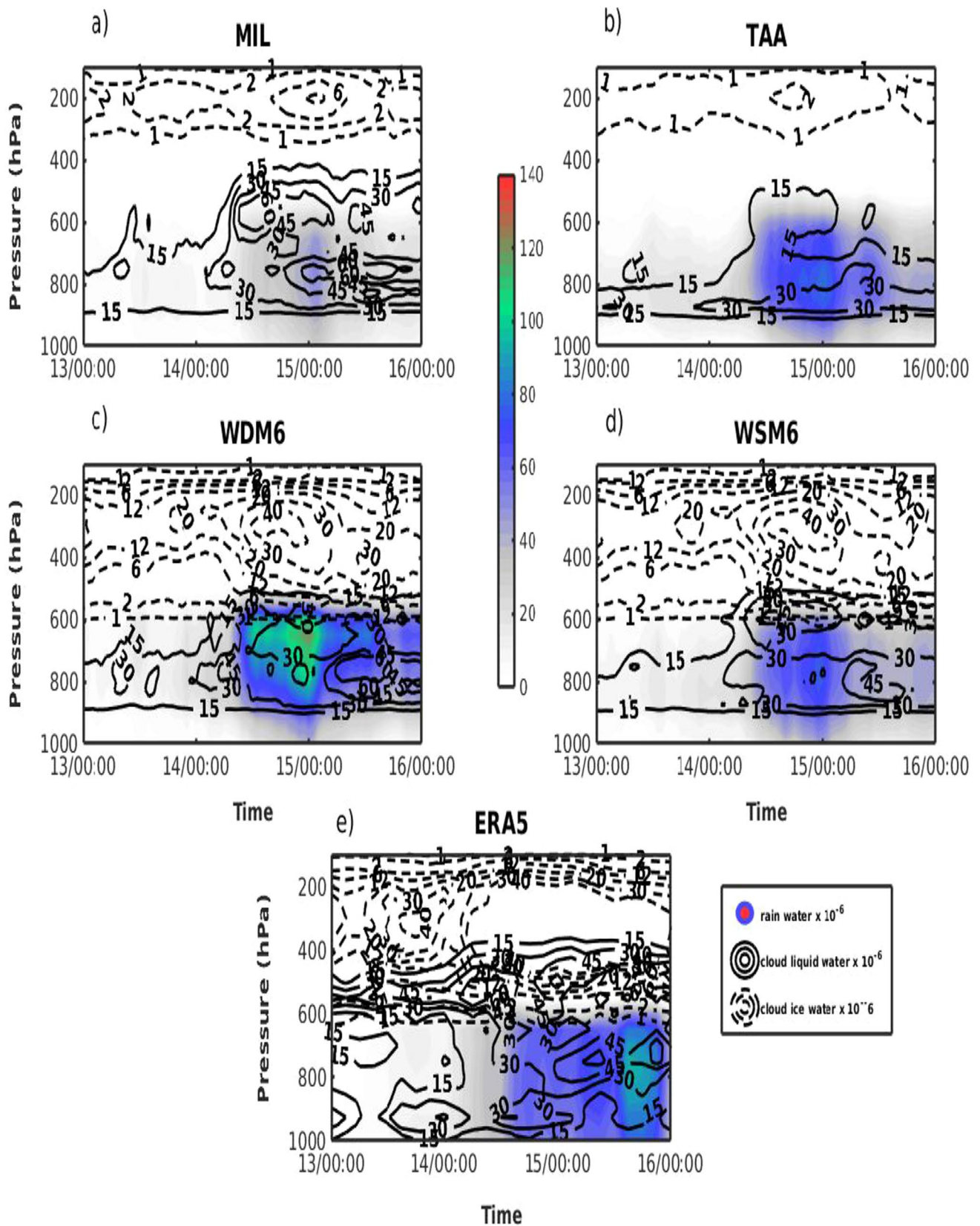
**Fig. 6** a–e CRAs predicted by different schemes along with the GPM for the total 3 days (day-2 to day-4) accumulated rainfall. The three different colours represent the three different features of rainfall obtained from GPM and the features identified by the different CMP

schemes are coloured based on the similarity of those features with respect to the respective feature of GPM. The three error components for the features identified by the different CMP schemes are calculated with respect to the respective GPM feature

cloud ice, which in turn decreased the cloud ice content. The graupel produced by TAA was negligible with respect to the other schemes; hence the graupel distribution for TAA has been omitted. Hence, from the hydrometeor analysis, it is evident that the prediction of upper-level frozen hydrometeors has a huge influence on the rainfall forecast. These results suggest that mixed-phase processes played a dominant role in this HRE and the inability of MIL and TAA to capture the cold rain component contributed hugely to the decrease in skills of rainfall prediction for these two schemes on the days of heaviest rainfall (day-3 and day-4). The lack of frozen hydrometeors in the MIL and TAA simulations signify that the rainfall produced by these two schemes throughout the course of simulation was majorly driven by warm rain processes. On the other hand, WDM6 and WSM6 were able to capture the development of frozen hydrometeors, thus capturing the cold rain component, which led to the relatively realistic simulation of rainfall by these two

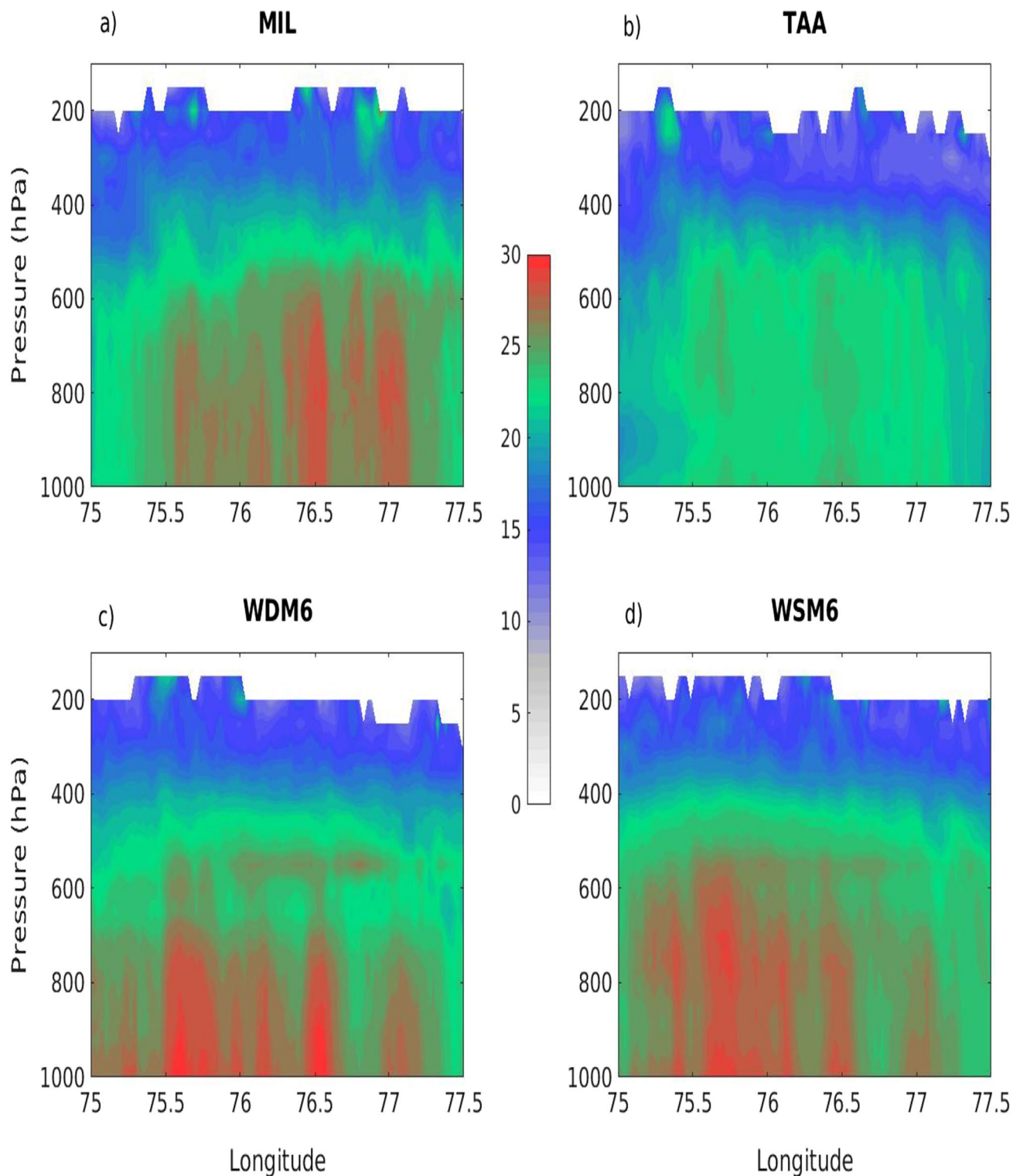
schemes. Besides, WDM6 and WSM6 have the tendency to hold precipitation hydrometeors (i.e., rainwater, cloud snow, graupel) without precipitating them instantaneously, and this might have facilitated more accumulation of frozen hydrometeors at the upper level. In addition to that, the warm rain component is better simulated by WDM6 as, being a double moment scheme, it can realistically simulate the number concentration of the cloud condensation nuclei (CCN), cloud droplet, and raindrop (Zhang et al. 2018). Hence, capturing the warm rain component better than WSM6 must have led WDM6 to have a higher skill of rainfall prediction than WSM6 on the days of the heaviest rainfall (day-3 and day-4).

Figure 8 shows the spatial average of model-derived radar reflectivity along longitudes against pressure levels over the inner domain for all the CMP schemes for day-3. It is evident that strong updraft motions and high hydrometeor activity till the mid-levels are better predicted by WDM6, WSM6, and MIL (Fig. 8a, c and d), wherein



**Fig. 7** a–e Spatial averaged time series of the mixing ratios of hydrometeors over the analysis polygon (Fig. 1): (1) cloud liquid water (solid contours), (2) cloud ice water (dotted contours) and (3) rain water (shading). All of the mixing ratios are scaled by  $10^6$  and unit is  $\text{kg kg}^{-1}$





**Fig. 8** a–d Latitudinal averaged vertical cross section of the model derived radar reflectivity over the inner domain on day-3

TAA poorly represented these key features (Fig. 8b). For MIL, high reflectivity zones ( $> 30$  dBz) are found at 500–600 hPa levels. High reflectivity is prominently visible at the lower as well as mid-levels in the WDM6.

The column integrated radar reflectivity as simulated by the model has been validated with the observations of the IMD Doppler Weather RADAR (DWR) situated at Kochi ( $9.93^{\circ}$  N,  $76.26^{\circ}$  E) for two time instants, i.e., 1200 UTC

of day-3 (14 August) and day-4 (15 August) (Fig. 9). The DWR captured scattered zones of high reflectivity (30–50 dBz) in the eastern and northern portions of the state of Kerala on day-3 (Fig. 9e). On day-4 a zone high reflectivity stretching from the adjacent sea to the middle portion of the state of Kerala is seen in the DWR (Fig. 9j). All the CMP schemes captured zones of high reflectivity (> 30 dBz) in the northern portion on day-3, and the strongest (weakest) zones of reflectivity were captured by WDM6 (TAA) (Fig. 9c and b). The WDM6 (WSM6 to some extent) captures the high reflectivity zones stretching from the northern to the southern portion of Kerala on day-4, but, the cluster of zones of high reflectivity at the middle of the state of Kerala (9.5–10.5° N), as shown by the DWR, was best captured by WDM6 on day-4 (Fig. 9h).

Though the locations of zones of higher reflectivity values were captured by MIL and TAA, the magnitude of reflectivity was significantly underestimated by TAA on both the days.

To further analyze the hydrometeor activity at different levels and to thoroughly investigate the nature of updraft for WDM6, WSM6 and MIL, the CFAD (Yuter and Houze 1995) with the model-derived radar reflectivity for all the CMP schemes over the analysis polygon (Fig. 1) are shown for day-2, day-3, and day-4 (Fig. 10). CFAD analysis helps us to locate the level of maximum reflectivity which indicates the zones of maximum microphysical activity, and thus provides a huge insight in the understanding of the inherent structure of hydrometeors in the atmosphere. MIL shows higher reflectivity near the surface compared to upper layers

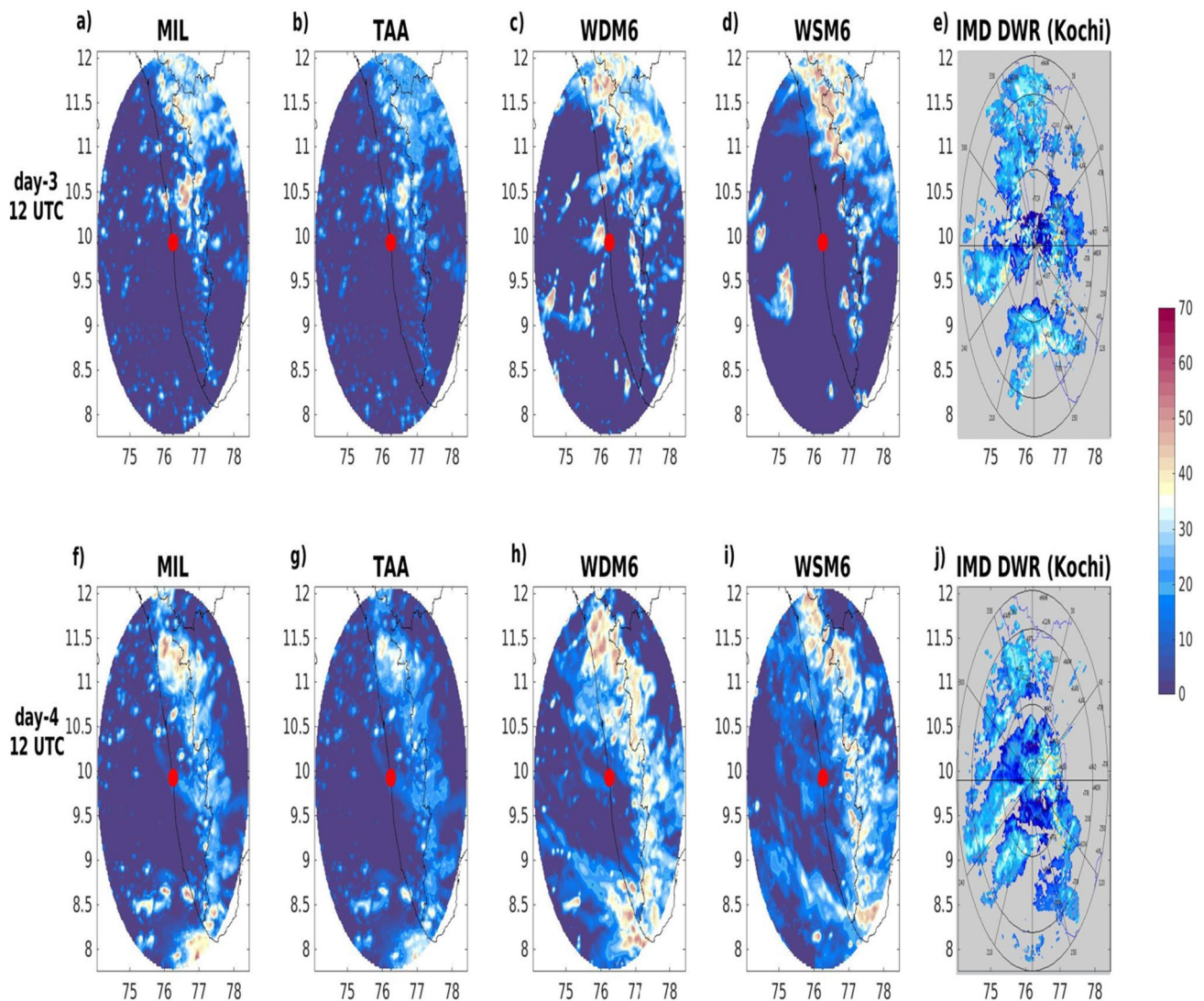


**Fig. 9** The model-produced radar reflectivity for all the CMP schemes along with the observations of the IMD Doppler Weather RADAR situated at Kochi (9.93° N, 76.26° E) at 1200 UTC of day-3

(14 August 2018) (a–e) and day-4 (15 August 2018) (f–j). The red spot indicates the location of the DWR at Kochi

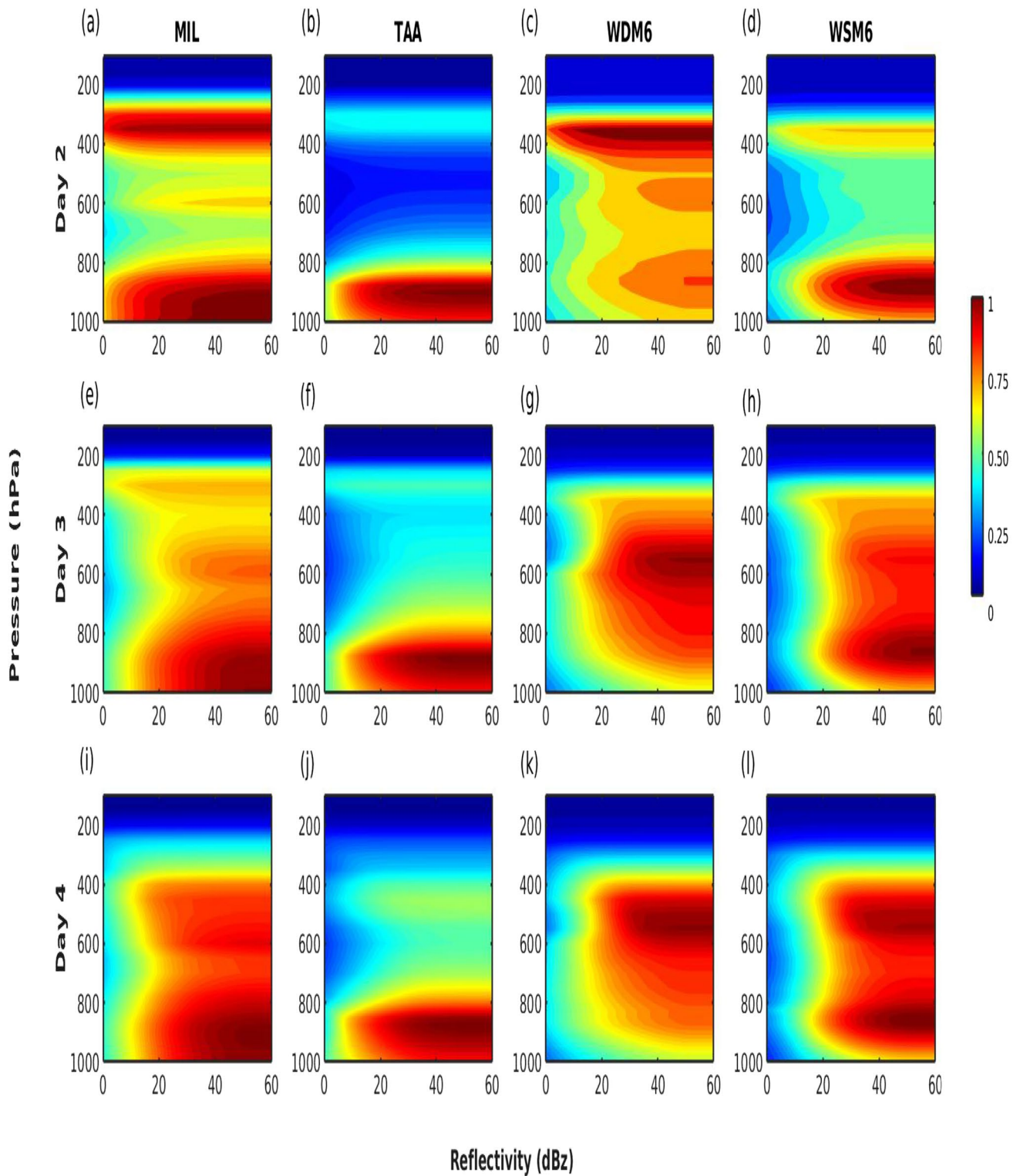


**Fig. 10 a–h** Contour Frequency Altitude Diagram (CFAD) of model-simulated radar reflectivity (dBz) for all the CMPs for all the days over the analysis polygon (Fig. 1). Contours represent frequency of

radar reflectivity relative to the maximum absolute radar reflectivity in the model derived data samples

throughout the simulation duration. This explains the lack of upper-level ice predicted by the scheme. TAA failed to capture the reflectivity at the upper levels (Fig. 10b, f and j). WDM6 shows the highest reflectivity (> 40 dBZ) contours at the upper levels (200 hPa) on day-2, but these highest reflectivity contours are seen at middle levels (500–600 hPa) on day-3 and day-4. This high reflectivity at the middle level in spite of the high amount of rainwater in the lower levels, indicates the domination of phase-change processes in the middle atmosphere. On day-2, for WSM6, very high reflectivity contours are noted at the lower levels, whereas for day-4 these high reflectivity patterns are visible at both the upper and lower levels (Fig. 10l). The CFAD of MIL suggests that the zone of maximum reflectivity stays near the ground, which is indicative of high liquid water content at the lower levels resulting in the dominance of warm rain processes. Similarly, TAA fails to capture the higher level reflectivity due to the absence of cloud ice at the upper levels. The WSM6 and the MIL scheme show similar CFADs with the higher levels showing higher reflectivity contours on day-3 and day-4. However, the reflectivity contours are attributed to cloud liquid water for MIL and cloud ice for WSM6.

### 3.4 Vertical velocity and temperature

Pressure–time plots for the differences of the spatial averaged vertical motion i.e. omega ( $\text{Pas}^{-1}$ ) for all the schemes over the analysis polygon (Fig. 1) with respect to WDM6 from day-2 to day-4 are shown in Fig. 11. It is evident that MIL is not able to capture the updraft motion at all with respect to (w.r.t.) WDM6 (Fig. 11a). Though there are similar updraft pattern for TAA (Fig. 11b) w.r.t. WDM6 in the lower levels (upto 700 hPa) for day-3. This lack of vertical velocity in the mid-levels inhibited the transport of water vapor and liquid hydrometeors to higher levels. WSM6 has shown resemblance in vertical velocity magnitudes to WDM6 (Fig. 11c). Similar plots for specific humidity and moisture convergence are shown in Figs. 12 and 13. It is evident that all the schemes simulated less specific humidity in the lower levels than WDM6 (Fig. 12) from day-2 to day-4. However, TAA and WSM6 showed higher specific humidity in the low levels (up to 850 hPa) than WDM6 for the entire simulation duration. This is corroborated by Fig. 13, where we see TAA and WSM6 showing higher surface moisture convergence than WDM6 on day-3 and day-4, whereas MIL couldn't capture the peaks except for one at the beginning of day-4.

Pressure–time plots for the differences of the spatial averaged temperature (K) for all the schemes over the analysis polygon (Fig. 1) w.r.t. WDM6 from day-2 to day-4 are shown in Fig. 14. It is evident that over the region, the upper-level temperature is warm for TAA and MIL

w.r.t WDM6 (Fig. 14a and b), which creates a less favourable environment for the generation of frozen hydrometeors. However, the difference in temperature between WSM6 and WDM6 is marginal. This is in agreement with the frozen hydrometeor distribution as simulated by MIL and TAA compared to WDM6. The averaged latent heat time series for upper (200–100 hPa) and lower level (900–600 hPa) are shown in Fig. 15. Results suggest that even though the upper-level latent heat is not varying much in the different MFC scenarios, the lower level latent heating is strongly modulated by the fluctuations in MFC.

### 3.5 Moisture budget

The Moisture Flux Convergence (MFC) have been calculated following the methodology of Banacos et al. (2005). By vector identity, horizontal MFC can be written as

$$\text{MFC} = -\nabla \cdot (qV_h) = -V_h \cdot \nabla q - q \nabla \cdot V_h \quad (2)$$

$$\text{MFC} = \underbrace{-u \frac{\partial q}{\partial x} - v \frac{\partial q}{\partial y}}_{\text{Advection term}} - \underbrace{q \left( \frac{\partial u}{\partial x} + \frac{\partial v}{\partial y} \right)}_{\text{Convergence term}} \quad (2a)$$

where  $q, V_h, u$  and  $v$  stand for specific humidity, horizontal velocity vector, zonal velocity, and meridional velocity.

The advection term represents the horizontal advection of specific humidity, whereas the convergence term denotes the product of specific humidity and horizontal mass convergence.

In this study, the contributions of the different components of the moisture budget equation (Eq. 2a) are studied for the Kerala HRE for the threshold of 100 mm. The advection and convergence terms are calculated using the formulation in Eq. (2a). This TRMM 3B42 3-hourly rain rate data are plotted alongside the different terms of the moisture budget equation to better understand the correlation between the model-predicted moisture convergence and the rainfall observations at higher temporal intervals (Fig. 16). The peaks of the MFC are prominent for all the schemes, and the contribution from the advection term is negative. In all the cases, the contribution of the MFC term peaks before the increase in rain rate predicted by the model and TRMM. But for WDM6, peaks of MFC are the most consistent with the peaks of rain rate (Fig. 16c). The lead-lag analysis is also carried out over the analysis polygon (Fig. 1) and the results are shown in Fig. 17. The WSM6 shows the lag between increased rain rate and MFC to be 2 h, which is highest among all (Fig. 17b). MIL and TAA predicted the MFC leading the peaks of rainfall by 1 h, which is similar to WDM6. In addition, it is prominently visible that the MFC

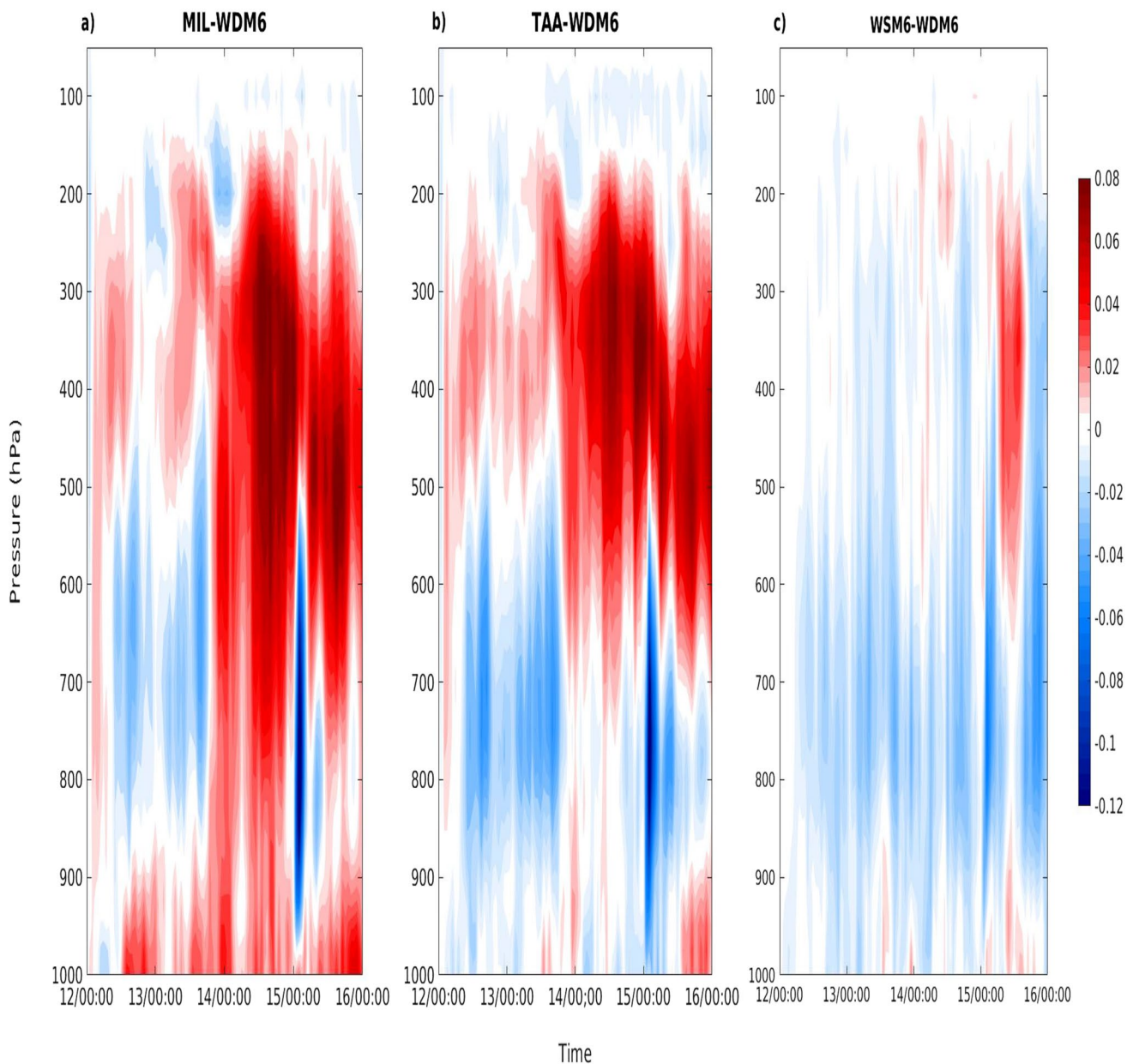


**Fig. 11** a–c Difference of spatial averaged time series of vertical velocity omega ( $\text{Pa s}^{-1}$ ) calculated over the analysis polygon (Fig. 1) for all the schemes with respect to WDM6

peaks are synchronized with the model-simulated rain-rate peaks in day-3 and day-4 for WDM6 and WSM6 (Fig. 17a).

From the moisture convergence scenario, it is seen that MIL simulated less moisture convergence than WDM6 almost throughout the course of the simulation (Fig. 13). Hence the accumulation of specific humidity at the lower levels is much less than WDM6, except for the beginning of day-4 when there was a momentary peak in moisture convergence in MIL than WDM6. This sudden increase of moisture convergence also resulted in the formation of relatively higher cloud ice formation than day-3 and also

justified the patch of higher latent heat for MIL during a few initial hours of day-4. However, the significant lack of moisture convergence is one of the key factors attributed to the substantial reduction in latent heat release for MIL as compared to WDM6. In addition, weaker surface convergence resulted in weaker updrafts that led to the formation of fewer amounts of frozen hydrometeors in MIL compared to WDM6; this is due to the fact that weaker updrafts (MIL) couldn't transport the low-level liquid hydrometeors to upper levels as seen in WDM6. In addition, the rain water content simulated by MIL is much less than WDM6, leading to poor

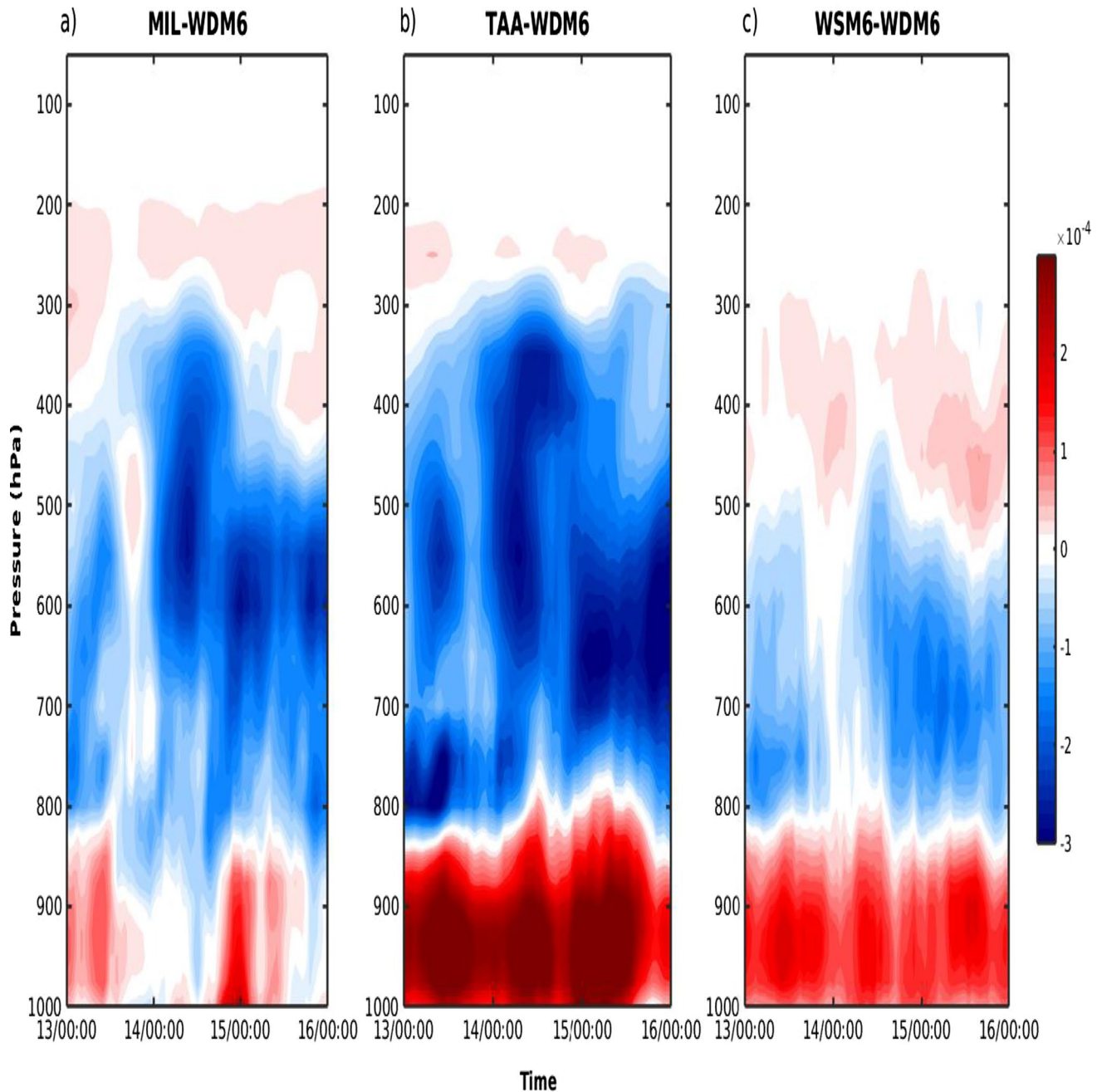


**Fig. 12** a–c Same as Fig. 11, but for specific humidity ( $\text{kg kg}^{-1}$ )

skills in rainfall prediction. On the other hand, in TAA, up to day-3, the vertical velocity structure is similar to that of WDM6 (Fig. 11); however, afterward, strong inhibition of updraft is noted in TAA compared to WDM6, leading to the poor simulation of frozen hydrometeors realistically. Simultaneously, the restriction in vertical transport of cloud liquid water and large accumulation of rainwater in TAA suggests that the autoconversion process might have played a key role in producing rainwater from cloud liquid water at the lower levels. Furthermore, TAA is not able to capture the

graupel like any other schemes; hence the rainfall simulated by TAA is mostly due to the warm rain process. Analysis of temperature (Fig. 14) and latent heat (Fig. 15) results clearly suggest that the MFC is strongly influencing the low level as well as the upper level hydrometeor distribution, rainfall, and the latent heating, and in turn modulating the convection and precipitation over this region.

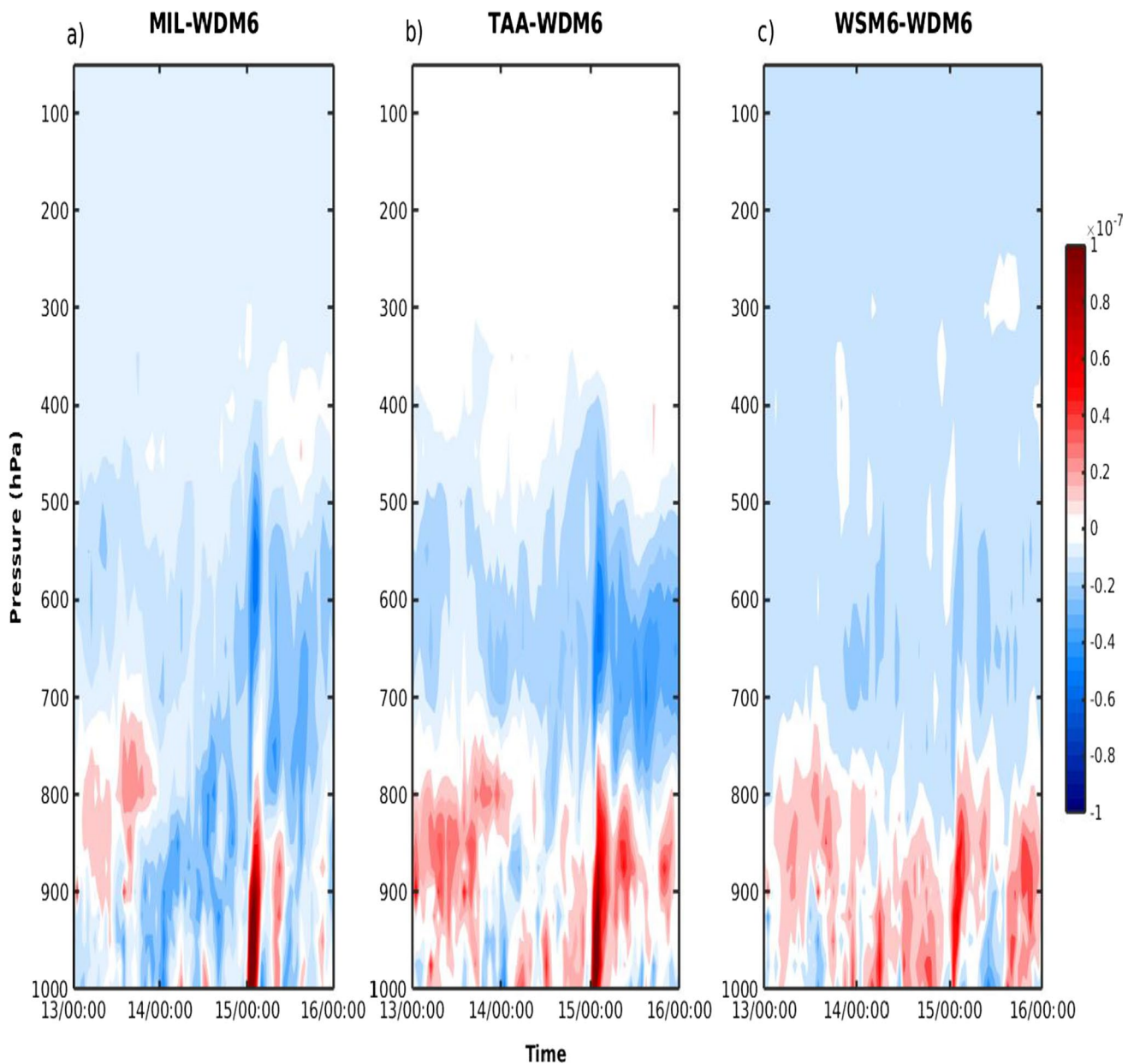


**Fig. 13** a–c Same as Fig. 11 but only for moisture convergence ( $\text{kg kg}^{-1} \text{s}^{-1}$ )

### 3.6 Orographic influence

To understand the influence of the orographic scenario in this HRE, the day-3 averaged cross sectional vertical velocity along with the cloud liquid water and cloud ice is plotted (the cross-sectional orography is shaded) for the latitudes of Kochi ( $10.15^\circ$ ), situated in the middle of the state (Fig. 18), and Thiruvananthapuram ( $8.47^\circ$ ), situated in the southern Kerala (Figure not shown). It is evident from Fig. 18 that the Western Ghats played an important role in the occurrence of this HRE. The moisture

convergence patches present beyond the coast of Kerala implies the accumulation of the moisture in the foothills of the orographic scenario. This accumulated moisture is transported to the upper atmosphere by means of orographic lifting facilitated by the windward slope of the Western Ghats. In Fig. 18, we can see that all the schemes show updraft motion in the windward slope. However, WDM6 shows the strongest updraft among the four CMP schemes. The cloud ice distribution confirms the lack of frozen hydrometeors formation by MIL and TAA. A downdraft motion is also seen in the leeward side of the Western Ghats, which is corroborated by the divergence patches in

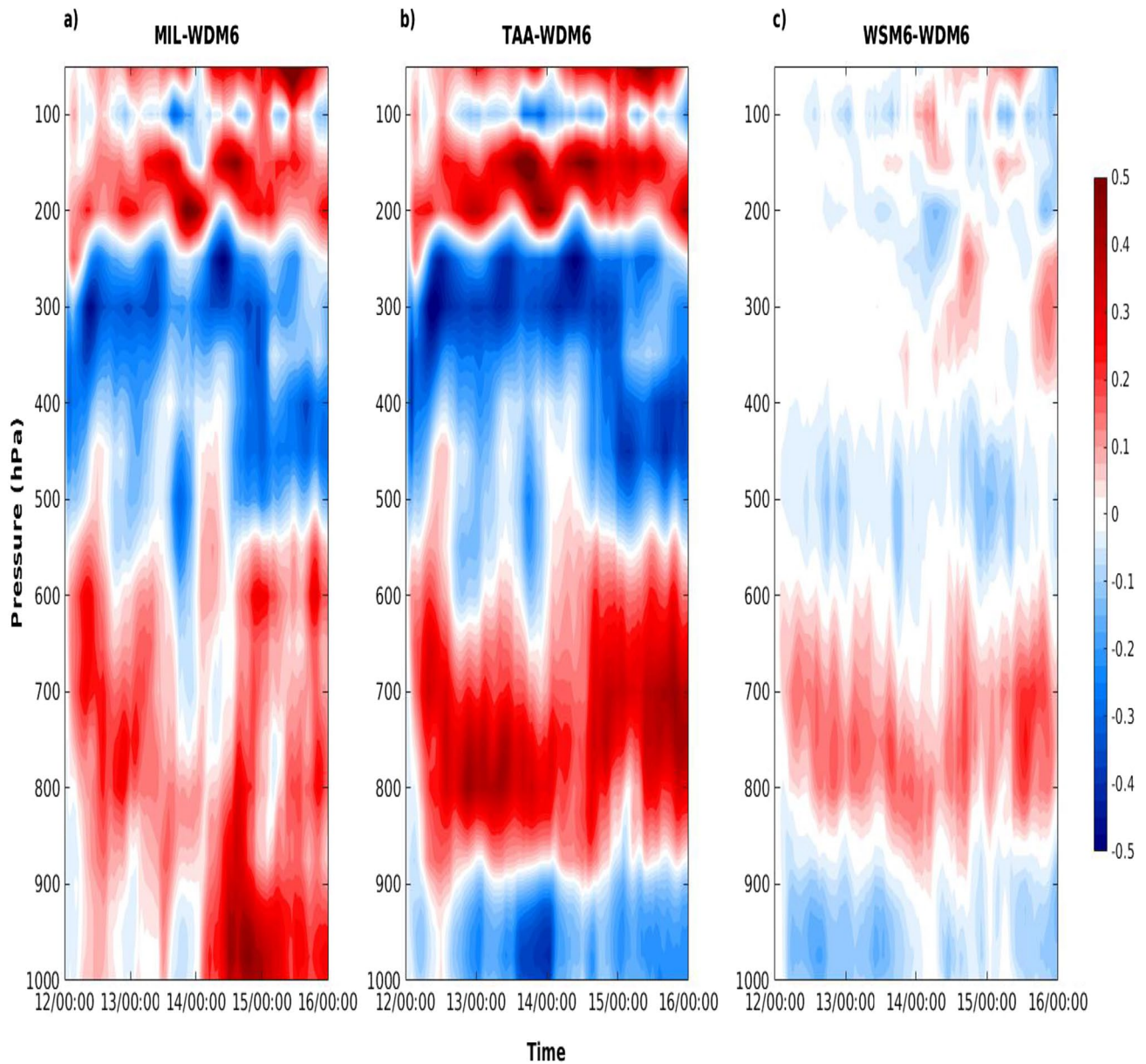


**Fig. 14** a–c Same as Fig. 11, but for temperature (K)

the eastern longitudes. A similar picture is also seen for the other station, i.e., Thiruvananthapuram.

## 4 Conclusions

Numerical simulations are carried out for the Kerala HRE (2018) using WRF-ARW model by employing four different CMP schemes, viz., MIL, TAA, WDM6, and WSM6. The 3AR for each experiment is validated against IMD station observations. It is found that WDM6 (TAA) has the best (worst) forecast skills among the suite of CMPs. The

differences of 3AR have increased for all the schemes due to the underestimation of rainfall at most of the stations on day-4. However, the WDM6 rainfall forecast for day-3 is close to IMD. WDM6 predicted 3AR with less than 100 mm difference at 22 out of the 31 stations considered for validation. This clearly implies that WDM6 is the best CMP scheme among the others for the heavy rainfall prediction in this scenario. Furthermore, the spatial distribution of rainfall over the land as predicted by the WDM6 and WSM6 is consistent with the GPM observations, whereas predictions from MIL and TAA are poor. For the days with the heaviest rainfall (day-3 and day-4), WDM6 shows higher skill



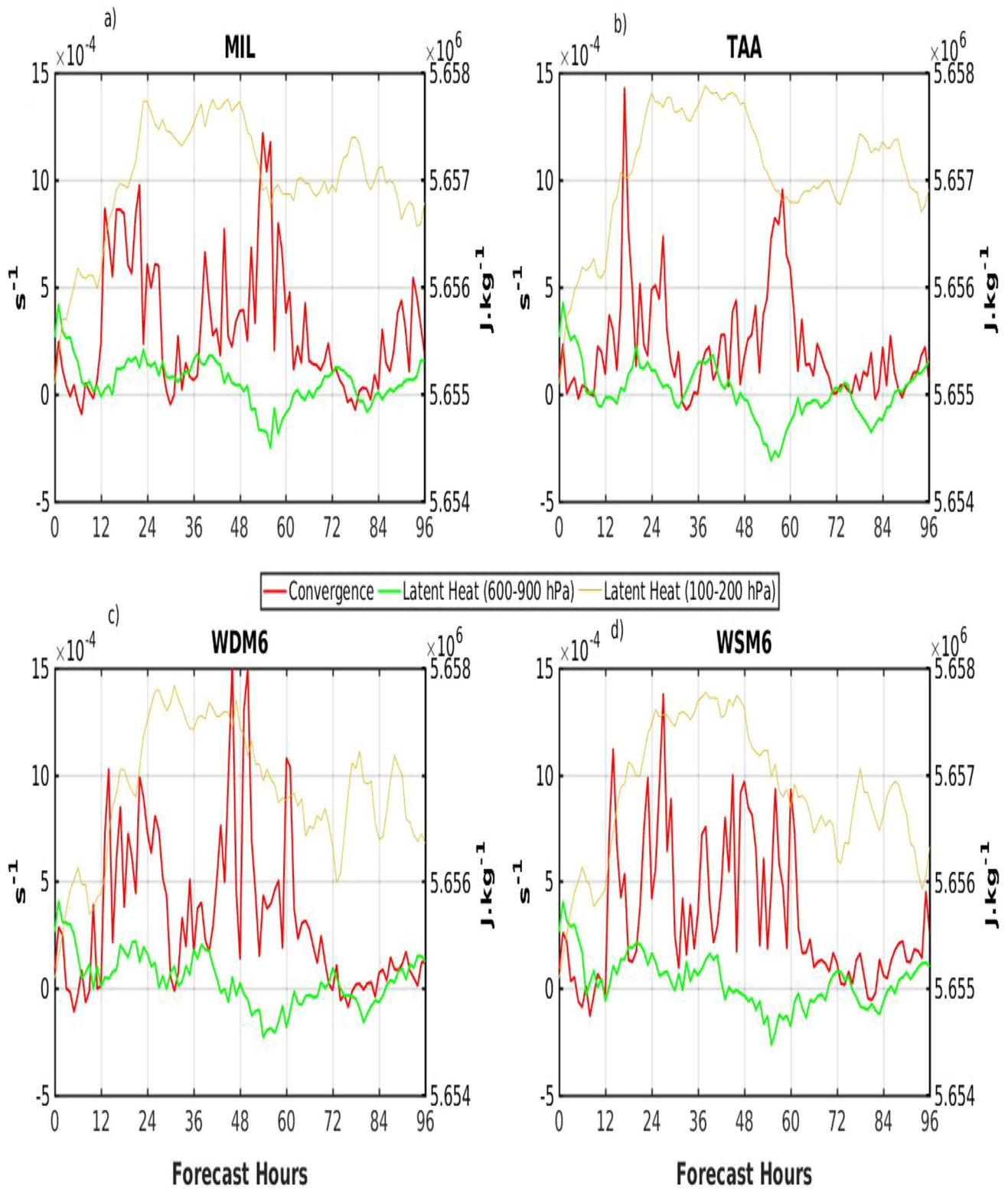


**Fig. 15** a–d Time series of the (1) MFC ( $\text{s}^{-1}$ ), (2) latent heat averaged between 600–900 hPa ( $\text{J kg}^{-1}$ ) and (3) latent heat averaged between 100–200 hPa ( $\text{J kg}^{-1}$ ) over the analysis polygon (Fig. 1)

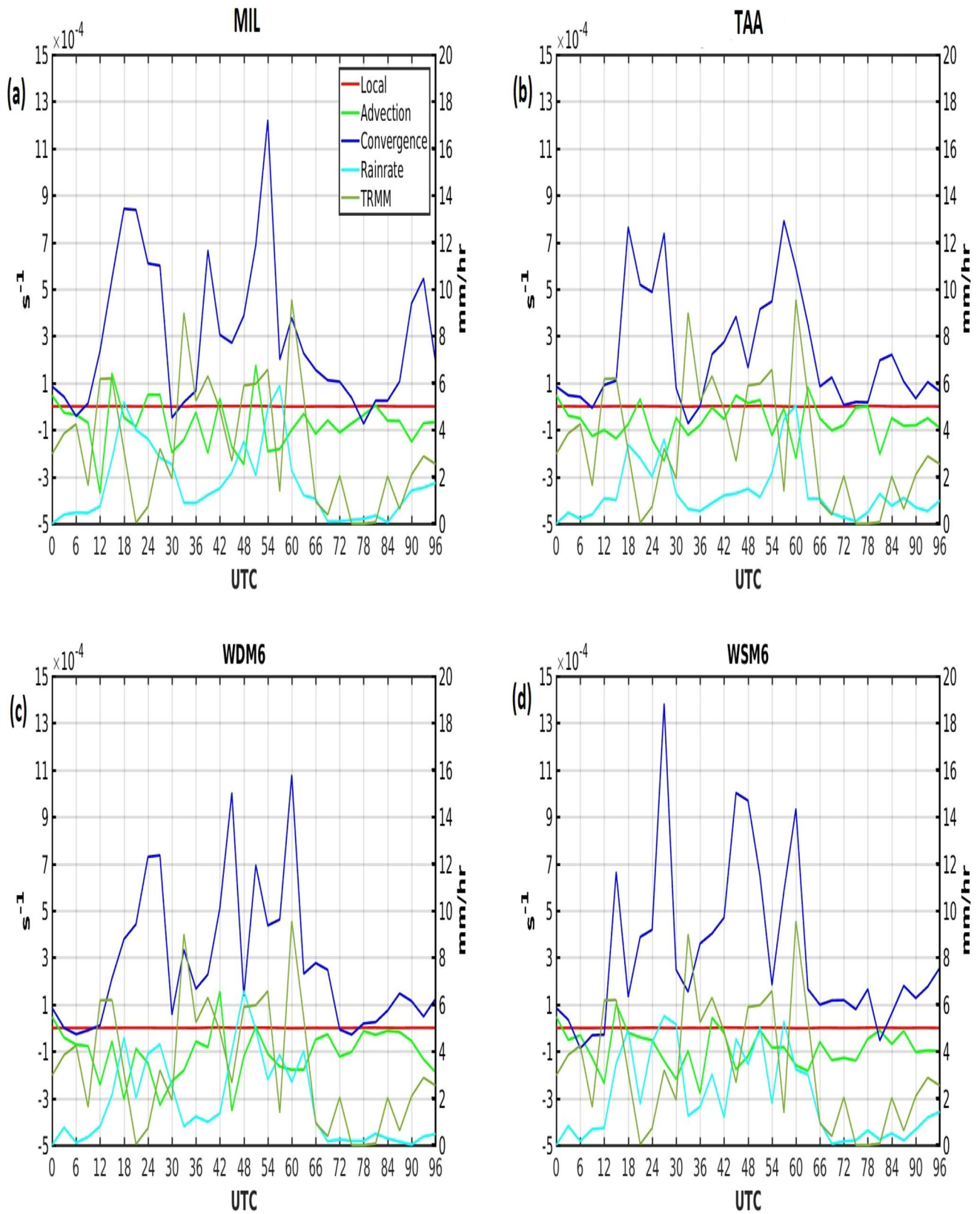


**Fig. 16** a–d Time series of the different components of the moisture budget equation, viz., (1) MFC ( $s^{-1}$ ), (2) local term, (3) advection term for 100 mm threshold along with the model predicted rain rate ( $mm\ h^{-1}$ ) and TRMM

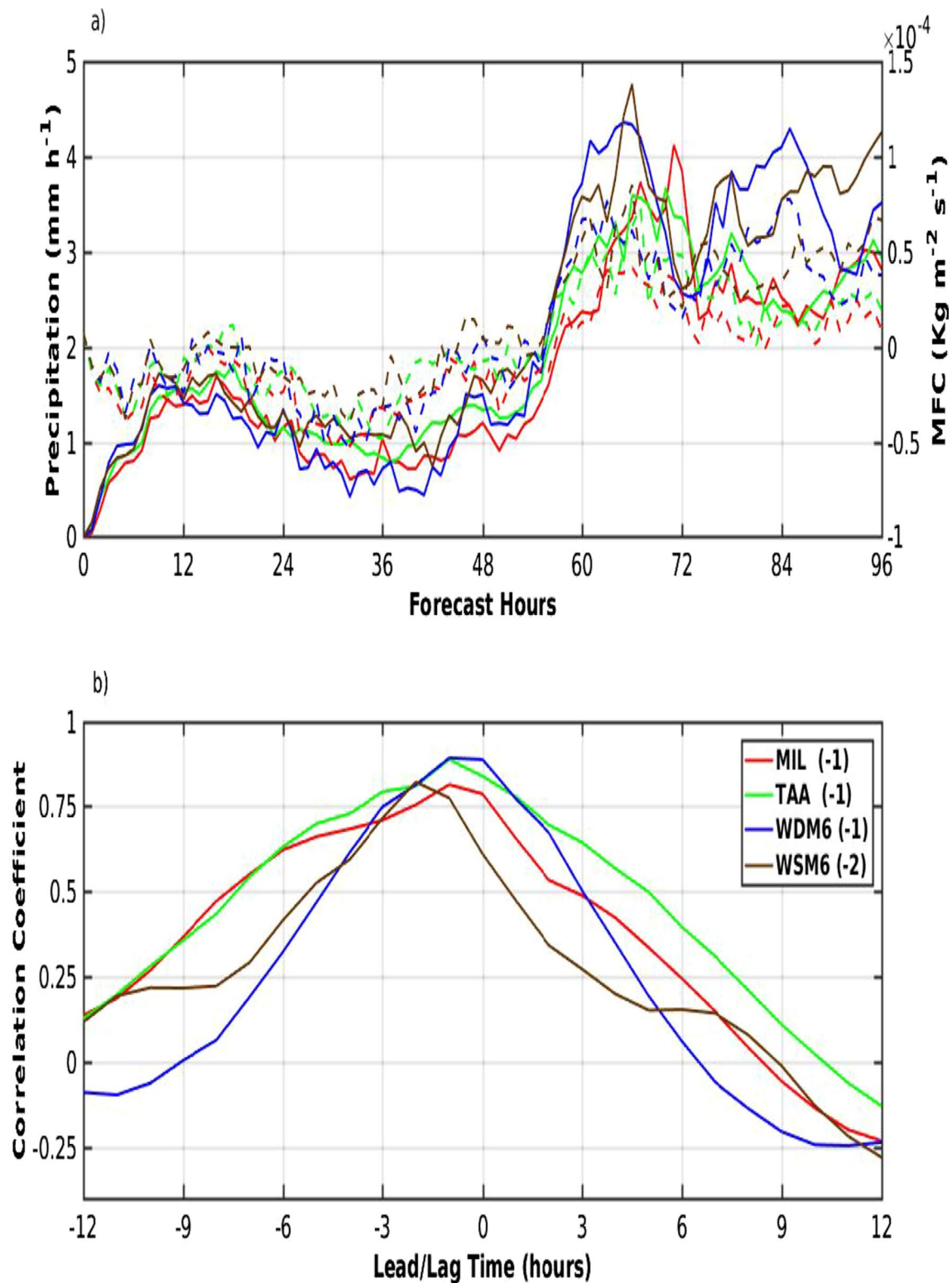


**Fig. 17** a, b Time series of a MFC (dotted lines) and rainrate (solid lines) for all the schemes (above) along with b the lead-lag correlation (including lag between MFC and rainrate, calculated over the

analysis polygon shown in Fig. 1) for all the schemes. The colours represent the corresponding CMP schemes according to the legend of (b)

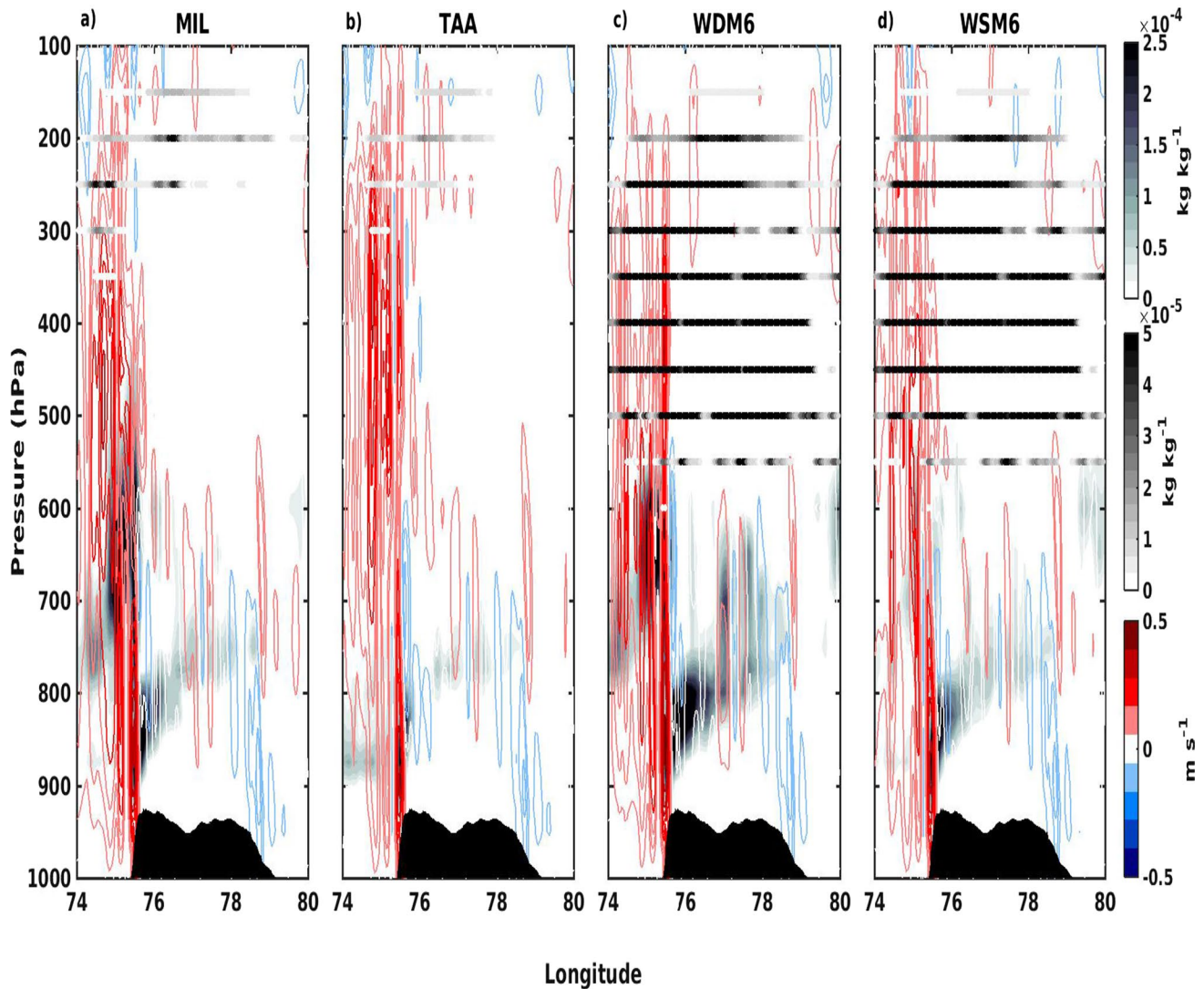


**Fig. 18 a–d** Averaged cloud liquid water (shaded, top colorbar) and cloud ice water (dotted, middle colorbar) overlaid with vertical velocity (contours, bottom colorbar) at the latitude of Kochi ( $10.15^{\circ}$  N)

for all the CMP schemes on day-3. The cross sectional orography is shaded and is plotted from 1000 hPa

in all the thresholds (10–150 mm). The CRA analysis has been conducted to find the decomposed errors for all the CMP schemes by keeping the threshold as 150 mm for CMP experiments and GPM. The CRA identified by WDM6 had moderate displacement and pattern errors, but the volumetric error was least among all the experiments.

From the hydrometeor analysis, it is prominent that the inability of MIL and TAA to simulate the frozen hydrometeors in the upper levels affected their rainfall prediction badly, resulting in poor skills. However, hydrometeors simulated by WDM6 and WSM6 are in agreement with the ERA5 data. The realistic simulation of frozen hydrometeors led these schemes to have a much better rainfall prediction than MIL and TAA. WDM6, being the double moment scheme, captured the warm rain processes

better than the WSM6, which led to its higher accuracy than WSM6. The latitudinal averaged vertical cross section of reflectivity showed zones of high updraft in MIL, WDM6 and WSM6, with WDM6 showing the strongest updrafts. Also, the comparison of model-simulated radar reflectivity with the IMD DWR observations suggests that the strongest (weakest) zones of reflectivity were captured by WDM6 and WSM6 (TAA) on both day-3 and day-4. However, the cluster of zones of high reflectivity on day-4 at the middle portion of Kerala ( $9.5\text{--}10.5^{\circ}$  N) was captured by WDM6, which is in agreement with the IMD DWR observation. Furthermore, the CFAD analysis of model-produced radar reflectivity showed that the hydrometeor activities were restricted to the lower level for MIL, which in turn, agrees with the lack of frozen hydrometeors in

the MIL simulations, but presence of enough cloud liquid water in the lower levels. In the case of WDM6, the domination of phase-change processes in the middle atmosphere is prominently visible, strengthening the indication that the cold rain processes were properly captured by WDM6.

Analysis of the moisture budget indicated that there is a significant impact of MFC in the rainfall prediction. In all the schemes, MFC led the rainrate peaks. The highest lead time was seen in WSM6 (2 h), whereas, for all the other simulations, it was 1 h. WDM6 simulated the MFC peaks in consistency with the TRMM rain rate. The peaks of moisture convergence can be associated with the convergence patterns visible beyond the coast of Kerala, in the foothills of Western Ghats. Orographic lifting played an important role in transporting the moisture to higher levels. There are patches of high moisture divergence along the leeward side of the Western Ghats indicating strong downdraft along the slope of the mountain. The results demonstrate that MFC plays an important role in accumulation of the moisture in lower and middle levels with further aggravation by the orographic presence. WDM6 captured the strongest updraft among all these experiments and this characterized with the adequate moisture leading to the better rainfall forecast skills. Furthermore, the better rainfall prediction skills of WDM6 is mainly attributed to, the accurate representation of frozen as well liquid hydrometeors facilitating a realistic simulation of both warm and cold rain processes.

This study provides the characteristic baseline behavior of key microphysical parameters and processes during a HRE in the complex geomorphological scenario over the southern Indian peninsular. However, investigation of this kind of meteorological event is highly influenced by several other factors (choice of boundary layer and cumulus convection parameterizations, resolution of the model domain etc.). Hence there is scope for further research for increasing the accuracy of the forecast for events such as this HRE. It is evident from researches such as this one, and the ones by Rajesh et al. (2017) and Mohan et al. (2018), that WRF has the capability of simulating HREs with reasonable accuracy over the Indian subcontinent, may it be the Hilly regions of Uttarakhand, or a coastal city in the eastern coast India, or a state with an orographic scenario in the Western coast of the country. It is anticipated that the findings of this research will be highly beneficial to operational forecasters, policy planners, and disaster risk managers for better prediction and preparedness to minimize the losses during these kinds of extreme HREs.

**Acknowledgements** The authors are grateful to the Indian Institute of Technology Bhubaneswar for providing the infrastructure to carry out this research work. The authors acknowledge the funding support from the University Grants Commission (UGC) (Grant number A18ES09002) and the Science and Engineering Research Board

(SERB) (Grant number RP-193), Government of India. The authors also acknowledge NCEP for the FNL/GDAS data used as the initial and boundary condition for the simulations. The authors are also grateful to the National Aeronautics and Space Administration (NASA) Earth Data for providing the GPM Final Run observations and TRMM 3B42 3-hourly rainfall data. The figures have been created using MATLAB ([www.mathworks.com](http://www.mathworks.com)), and the algorithms are available upon request to the corresponding author.

## References

- Agnihotri G, Dimri AP (2015) Simulation study of heavy rainfall episodes over the southern Indian peninsula. *Meteorol Appl* 22:223–235. <https://doi.org/10.1002/met.1446>
- Ahern M, Kovats RS, Wilkinson P, Few R, Matthies F (2005) Global health impacts of floods: epidemiologic evidence. *Epidemiol Rev* 27:36–46. <https://doi.org/10.1093/epirev/mxi004>
- Ault AP, Williams CR, White AB, Neiman PJ, Creamean JM, Gaston CJ, Ralph FM, Prather KA (2011) Detection of Asian dust in California orographic precipitation. *J Geophys Res* 116:D16205. <https://doi.org/10.1029/2010JD015351>
- Baisya H, Pattnaik S (2019) Orographic effect and multiscale interactions during an extreme rainfall event. *Environ Res Commun* 1:051002. <https://doi.org/10.1088/2515-7620/ab2417>
- Banacos PC, Schultz DM, Banacos PC, Schultz DM (2005) The use of moisture flux convergence in forecasting convective initiation: historical and operational perspectives. *Weather Forecast* 20:351–366. <https://doi.org/10.1175/WAF858.1>
- Breiland JG (1958) Meteorological conditions associated with the development of instability lines. *J Meteorol* 15:297–302. [https://doi.org/10.1175/1520-0469\(1958\)015%3c0297:MCAWD%3e2.0.CO;2](https://doi.org/10.1175/1520-0469(1958)015%3c0297:MCAWD%3e2.0.CO;2)
- Chen Y, Ebert EE, Davidson NE, Walsh KJE (2018) Application of contiguous rain area (CRA) methods to tropical cyclone rainfall forecast verification. *Earth Space Sci*. <https://doi.org/10.1029/2018EA000412>
- Dasari HP, Salgado R, Perdigao J, Challa VS (2014) A regional climate simulation study using WRF-ARW model over Europe and evaluation for extreme temperature weather events. *Int J Atmos Sci* 2014:1–22. <https://doi.org/10.1155/2014/704079>
- Dodla VBR, Ratna SB (2010) Mesoscale characteristics and prediction of an unusual extreme heavy precipitation event over India using a high resolution mesoscale model. *Atmos Res* 95:255–269. <https://doi.org/10.1016/j.atmosres.2009.10.004>
- Dudhia J (1989) Numerical study of convection observed during the winter monsoon experiment using a mesoscale two-dimensional model. *J Atmos Sci* 46:3077–3107. [https://doi.org/10.1175/1520-0469\(1989\)046%3c3077:NSOCOD%3e2.0.CO;2](https://doi.org/10.1175/1520-0469(1989)046%3c3077:NSOCOD%3e2.0.CO;2)
- Ebert E, Gallus W (2009) Toward better understanding of the contiguous rain area (CRA) method for spatial forecast verification. *Weather Forecast* 24(5):1401–1415
- Ebert E, McBride J (2000) Verification of precipitation in weather systems: determination of systematic errors. *J Hydrol* 239:179–202. [https://doi.org/10.1016/S0022-1694\(00\)00343-7](https://doi.org/10.1016/S0022-1694(00)00343-7)
- Ghosh P, Ramkumar TK, Yesubabu V, Naidu CV (2016) Convection-generated high-frequency gravity waves as observed by MST radar and simulated by WRF model over the Indian tropical station of Gadanki. *Q J R Meteorol Soc* 142:3036–3049. <https://doi.org/10.1002/qj.2887>
- Grams J, Gallus W, Koch S (2006) The use of a modified Ebert-McBride technique to evaluate mesoscale model QPF as a function of convective system morphology during IHOP 2002. *Weather Forecast* 21:288

- Grubisic V, Vellore RK, Huggins AW (2005) Quantitative precipitation forecasting wintertime storms in the Sierra Nevada: sensitivity to the microphysical parameterization. *Mon Weather Rev* 133:2834–2859
- Hally A, Richard E, Fresnay S, Lambert D (2014) Ensemble simulations with perturbed physical parametrizations: pre-HyMeX case studies. *Q J R Meteorol Soc* 140:1900–1916. <https://doi.org/10.1002/qj.2257>
- Hersbach H, Bell B, Berrisford P, Biavati G, Horányi A, Muñoz Sabater J, Nicolas J, Peubey C, Radu R, Rozum I, Schepers D, Simmons A, Soci C, Dee D, Thépaut J-N (2018) ERA5 hourly data on pressure levels from 1979 to present. Copernicus Climate Change Service (C3S) Climate Data Store (CDS). <https://doi.org/10.24381/cds.bd0915c6>
- Hong SY, Pan HL, Hong SY, Pan HL (1996) Nonlocal boundary layer vertical diffusion in a medium-range forecast model. *Mon Weather Rev* 124:2322–2339. [https://doi.org/10.1175/1520-0493\(1996\)124%3c2322:NBLVDI%3e2.0.CO;2](https://doi.org/10.1175/1520-0493(1996)124%3c2322:NBLVDI%3e2.0.CO;2)
- Hong SY, Lim KSS, Lee YH, Ha JC, Kim HW, Ham SJ, Dudhia J (2010) Evaluation of the WRF double-moment 6-class microphysics scheme for precipitating convection. *Adv Meteorol* 2010:1–10. <https://doi.org/10.1155/2010/707253>
- Huang YC, Wang PK (2017) The hydrometeor partitioning and microphysical processes over the Pacific Warm Pool in numerical modeling. *Atmos Res*. <https://doi.org/10.1016/j.atmosres.2016.09.009>
- Huffman GJ et al (2007) The TRMM multi-satellite precipitation analysis (TMPA): quasi global, multiyear, combined-sensor precipitation estimates at fine scales. *J Hydrometeorol* 8(1):38–55
- Huffman GJ, Bolvin D, Braithwaite D, Hsu K, Joyce R, Xie P (2014) Integrated multi-satellite retrievals for GPM (IMERG), version 4.4. NASA's Precipitation Processing Center, <ftp://arthurhou.pps.eosdis.nasa.gov/gpmdata/>. Accessed 10 Dec 2020
- IMD Report (2018) Rainfall over Kerala during Monsoon Season-2018 and forecast for next 5 days. [www.imdvm.gov.in/images/rainfall%20over%20kerala%20during%20monsoon%20season-2018%20and%20forecast%20for%20next%205%20days.pdf](http://www.imdvm.gov.in/images/rainfall%20over%20kerala%20during%20monsoon%20season-2018%20and%20forecast%20for%20next%205%20days.pdf)
- John SK (2004) The Kain-Fritsch convective parameterization: an update. *J Appl Meteorol* 43:170–181. [https://doi.org/10.1175/1520-0450\(2004\)043<0170:TKCPAU>2.0.CO;2](https://doi.org/10.1175/1520-0450(2004)043<0170:TKCPAU>2.0.CO;2)
- Kaplan M, Vellore RK, Marzette PJ, Lewis JM (2012) The role of windward side diabatic heating in Sierra Nevada spillover precipitation. *J Hydromet* 13:1175–1194
- Kumar O, Suneetha P (2012) Simulation of heavy rainfall events during retreat phase of summer monsoon season over parts of Andhra Pradesh. [file.scirp.org. http://file.scirp.org/pdf/IJG2012040020\\_70895938.pdf](http://file.scirp.org/pdf/IJG2012040020_70895938.pdf)
- Lim J-OJ, Hong S-Y (2005) Effects of Bulk Microphysics on the Simulated Monsoonal Precipitation over East Asia. *J Geophys Res* 110:D24201. <https://doi.org/10.1029/2005JD006166>
- Lim KSS, Hong SY (2009) Development of an effective double-moment cloud microphysics scheme with prognostic cloud condensation nuclei (CCN) for weather and climate models. *Mon Weather Rev* 138:1587–1612. <https://doi.org/10.1175/2009mw2968.1>
- Matsumoto S, Ninomiya K, Akiyama T (1967) Cumulus activities in relation field to the mesoscale convergence. *J Met Soc Jpn* 45:292–305
- McCumber M, Tao WK, Simpson J, Penc R, Soong ST (2010) Comparison of ice-phase microphysical parameterization schemes using numerical simulations of tropical convection. *J Appl Meteorol*. <https://doi.org/10.1175/1520-0450-30.7.985>
- Milbrandt JA, Yau MK (2005) A Multimoment bulk microphysics parameterization. Part I: analysis of the role of the spectral shape parameter. *J Atmos Sci* 62:3051–3064. <https://doi.org/10.1175/JAS3534.1>
- Mlawer EJ, Taubman SJ, Brown PD, Iacono MJ, Clough SA (1997) Radiative transfer for inhomogeneous atmospheres: RRTM, a validated correlated-k model for the longwave. *J Geophys Res Atmos* 102:16663–16682. <https://doi.org/10.1029/97JD00237>
- Monin AS, Obukhov AM (1954) Basic laws of turbulent mixing in the atmosphere near the ground. *Tr Akad Nauk SSSR Geofiz Inst* 24:163–187
- Morrison H, Curry JA, Khvorostyanov VI, Morrison H, Curry JA, Khvorostyanov VI (2005) A new double-moment microphysics parameterization for application in cloud and climate models. Part I: description. *J Atmos Sci* 62:1665–1677. <https://doi.org/10.1175/JAS3446.1>
- NCEP: National Centers for Environmental Prediction/National Weather Service/NOAA/U.S. Department of Commerce (2015) NCEP GDAS/FNL 0.25 degree global tropospheric analyses and forecast grids. Research Data Archive at the National Center for Atmospheric Research, Computational and Information Systems Laboratory. <https://doi.org/10.5065/D65Q4T4Z>
- Niu GY, Yang ZL, Mitchell KE, Chen F, Ek MB, Barlage M, Kumar A, Manning K, Niyogi D, Rosero E, Tewari M, Xia Y (2011) The community Noah land surface model with multiparameterization options (Noah-MP). 1: Model description and evaluation with local-scale measurements. *J Geophys Res* 116:D12109. <https://doi.org/10.1029/2010JD015139>
- Pattanaik DR, Rajeevan M (2009) Variability of extreme rainfall events over India during southwest monsoon season. *Meteorol Appl*. <https://doi.org/10.1002/met.164>
- Peslen CA (1980) Short-interval SMS wind vector determinations for a severe local storms area. *Mon Weather Rev* 108:1407–1418. [https://doi.org/10.1175/1520-0493\(1980\)108%3c1407:SISWV D%3e2.0.CO;2](https://doi.org/10.1175/1520-0493(1980)108%3c1407:SISWV D%3e2.0.CO;2)
- Powers JG, Klemp JB, Skamarock WC, Davis CA, Dudhia J, Gill DO, Coen JL, Gochis DJ, Ahmadov R, Peckham SE, Grell GA, Michalakes J, Trahan S, Benjamin SG, Alexander CR, Dimego GJ, Wang W, Schwartz CS, Romine GS, Liu Z, Snyder C, Chen F, Barlage MJ, Yu W, Duda MG (2017) The weather research and forecasting model: overview, system efforts, and future directions. *Bull Am Meteorol Soc* 98:1717–1737. <https://doi.org/10.1175/BAMS-D-15-00308.1>
- Rajeevan M, Kesarkar A, Thampi SB, Rao TN, Radhakrishna B, Rajasekhar M (2010) Sensitivity of WRF cloud microphysics to simulations of a severe thunderstorm event over Southeast India. *Ann Geophys* 28:603–619. <https://doi.org/10.5194/angeo-28-603-2010>
- Rajesh PV, Pattanaik S, Rai D, Osuri KK, Mohanty UC, Tripathy S (2017) Role of land state in a high resolution mesoscale model for simulating the Uttarakhand heavy rainfall event over India. *J Earth Syst Sci* 125:475–498
- Reshmi Mohan P, Srinivas CV, Yesubabu V, Baskaran R, Venkatraman B (2018) Simulation of a heavy rainfall event over Chennai in Southeast India using WRF: sensitivity to microphysics parameterization. *Atmos Res* 210:83–99. <https://doi.org/10.1016/j.atmosres.2018.04.005>
- Saha K (1974) Some aspects of the Arabian sea summer monsoon. *Tellus* 26:464–476. <https://doi.org/10.1111/j.2153-3490.1974.tb01624.x>
- Skamarock C, Klemp B, Dudhia J, Gill O, Barker D, Duda G, Huang X, Wang W, Powers G (2008) A description of the advanced research WRF version 3. <https://doi.org/10.5065/D68S4MVH>
- Srinivas CV, Yesubabu V, Prasad DH, Hari Prasad KBRR, Greeshma MM, Baskaran R, Venkatraman B (2018) Simulation of an extreme heavy rainfall event over Chennai, India using WRF: sensitivity to grid resolution and boundary layer physics. *Atmos Res* 210:66–82. <https://doi.org/10.1016/J.ATMOSRES.2018.04.014>
- Tan E (2016) Microphysics parameterization sensitivity of the WRF model version 3.1.7 to extreme precipitation: evaluation of the

- 1997 New Year's flood of California. *Geosci Model Dev Discuss.* <https://doi.org/10.5194/gmd-2016-94>
- Taylor KE (2001) Summarizing multiple aspects of model performance in a single diagram. *J Geophys Res Atmos* 106:7183–7192. <https://doi.org/10.1029/2000JD900719>
- Thompson G, Eidhammer T (2014) A study of aerosol impacts on clouds and precipitation development in a large winter cyclone. *J Atmos Sci* 71:3636–3658. <https://doi.org/10.1175/jas-d-13-0305.1>
- Thompson G, Field PR, Rasmussen RM, Hall WD (2008) Explicit forecasts of winter precipitation using an improved bulk microphysics scheme. Part II: implementation of a new snow parameterization. *Mon Weather Rev* 136:5095–5115. <https://doi.org/10.1175/2008MWR2387.1>
- Vellore RK et al (2014) On the anomalous precipitation enhancement over the Himalayan foothills during monsoon breaks. *Clim Dyn* 43:2009–2031
- Vellore RK et al (2019) Sub-synoptic variability in the Himalayan extreme precipitation event during June 2013. *Meteorol Atmos Phys.* <https://doi.org/10.1007/s00703-019-00713-5>
- Vellore RK, Kaplan ML, Krishnan R, Lewis JM, Sabade S, Deshpande N, Singh BB, Madhura RK, Rama Rao MVS (2016) Monsoon-extratropical circulation interactions in Himalayan extreme rainfall. *Clim Dyn* 46:3517–3546. <https://doi.org/10.1007/s00382-015-2784-x>
- Viswanadhapalli Y, Srinivas CV, Basha G, Dasari HP, Langodan S, Ratnam MV, Hoteit I (2019) A diagnostic study of extreme precipitation over Kerala during August 2018. *Atmos Sci Lett* 20:e941. <https://doi.org/10.1002/asl.941>
- Wilks DS (ed) (2011) *Statistical methods in the atmospheric sciences.* International Geophysics, vol 100, pp 2–676
- Wilson JW, Meigenhardt DL (1997) Thunderstorm initiation, organization, and lifetime associated with Florida boundary layer convergence lines. *Mon Weather Rev* 125:1507–1525. [https://doi.org/10.1175/1520-0493\(1997\)125%3C1507:TIOALAE%3E2.0.CO;2](https://doi.org/10.1175/1520-0493(1997)125%3C1507:TIOALAE%3E2.0.CO;2)
- Wilson JW, Mueller CK (1993) Nowcasts of thunderstorm initiation and evolution. *Weather Forecast* 8:113–131. [https://doi.org/10.1175/1520-0434\(1993\)008%3c0113:NOTIAE%3E2.0.CO;2](https://doi.org/10.1175/1520-0434(1993)008%3c0113:NOTIAE%3E2.0.CO;2)
- Wilson JW, Schreiber WE (1986) Initiation of convective storms at radar-observed boundary-layer convergence lines. *Mon Weather Rev* 114:2516–2536. [https://doi.org/10.1175/1520-0493\(1986\)114%3c2516:IOCSAR%3E2.0.CO;2](https://doi.org/10.1175/1520-0493(1986)114%3c2516:IOCSAR%3E2.0.CO;2)
- Yuter SE, Houze RA (1995) Three-dimensional kinematic and microphysical evolution of Florida Cumulonimbus. Part II: frequency distributions of vertical velocity, reflectivity, and differential reflectivity. *Mon Weather Rev* 123:1941–1963. [https://doi.org/10.1175/1520-0493\(1995\)123%3c1941:TDKAME%3E2.0.CO;2](https://doi.org/10.1175/1520-0493(1995)123%3c1941:TDKAME%3E2.0.CO;2)
- Zhang M, Wang H, Zhang X, Peng Y, Che H (2018) Applying the WRF double-moment six-class microphysics scheme in the GRAPES\_Meso Model: a case study. *J Meteorol Res* 32:246–264. <https://doi.org/10.1007/s13351-018-7066-1>

**Publisher's Note** Springer Nature remains neutral with regard to jurisdictional claims in published maps and institutional affiliations.